University of Stuttgart

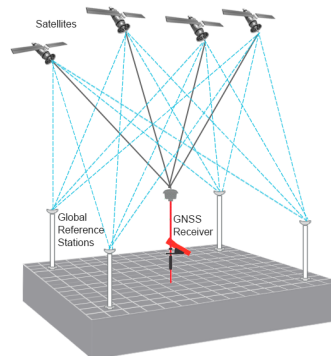Institute of Geodesy

BOSCH

Error Propagation and Integrity for Dual Frequency PPP with Carrier Cycle Ambiguity Resolution

Masterthesis im Studiengang

GEOENGINE

University of Stuttgart

Lu Chen

Stuttgart, February 2024

Examiner:	Dr.-Ing. Mohammad J. Tourian Universität Stuttgart
Supervisor:	Dr. Boubeker Belabbas Robert Bosch GmbH

Erklärung der Urheberschaft

Ich erkläre hiermit an Eides statt, dass ich die vorliegende Arbeit ohne Hilfe Dritter und ohne Benutzung anderer als der angegebenen Hilfsmittel angefertigt habe; die aus fremden Quellen direkt oder indirekt übernommenen Gedanken sind als solche kenntlich gemacht. Die Arbeit wurde bisher in gleicher oder ähnlicher Form in keiner anderen Prüfungsbehörde der Universität Stuttgart oder einer anderen Hochschule vorgelegt, und auch noch nicht veröffentlicht.

_____

Ort, Datum

_____

Unterschrift

Declaration of authorship

I declare in lieu of an oath, that the research reported within this thesis has been conducted by the author unless indicated otherwise. Ideas provided directly or indirectly by others have been marked for that. The material contained within this thesis has not previously been submitted for a degree to the examination authority of the University of Stuttgart or any other University, and is also not published otherwise.

Acknowledgments

Abstract

The emergence of precision point positioning (PPP), as a crucial advancement in the Global Navigation Satellite Systems (GNSS) positioning field, has fueled the search for faster, highly accurate, and user-friendly solutions, distinguishing it from traditional Real-time Kinematic (RTK), which heavily relies on reference stations. The availability of precision correction products, including accurate external clocks, ephemerides, and correction data provided by the International GNSS Service (IGS) or other commercial entities, has significantly expedited the advancement of PPP. Current research aims to shorten convergence time while preserving high accuracy. However, achieving this objective presents a challenge, as pursuing higher accuracy often necessitates a longer convergence time, making it a noteworthy research area.

This master's thesis aims to assess the sensitivity of Key Performance Indicators (KPIs) to correction product uncertainties, encompassing satellite orbit errors, satellite clock errors, and troposphere delay errors. The goal is to identify sources that exhibit heightened sensitivity to KPIs, allowing for the provision of recommendations to researchers on refining the accuracy of error correction products. Here, KPIs refer to convergence time, fixing rate, and position error. Two error models are introduced to emulate the dissemination of uncertainties originating from correction products. The focus is primarily on examining the influence of the correction product errors in pseudorange measurements on KPIs. The simulation involves the modeling of multipath and receiver noise using the Minimum Operational Performance Standards (MOPS) model. Additionally, the phase measurement noise is confined within a specified accuracy. The PPP Ambiguity Resolution algorithm (PPP AR) employed in this study is sourced from a Bosch research center, and a simulated dataset is utilized in a static mode simulation.

The numerical results offer insights into Monte Carlo simulation iterations, model comparisons, including differences in autocorrelation, and the impact of phase noise variation on the convergence time, fixing rate, and position error. Advocating for 100 runs as simulations within the studied cases, the findings suggest that there is sufficient stability in presenting statistical results related to the KPIs. The assumption is made that all standard deviations of the errors of interest are aligned with the line of sight. In the specified scenario of "Base", where only satellite clock errors have a standard deviation of 0.15 m, orbit errors standard deviation at 0.05 m, and the standard deviation of vertical troposphere errors is 0.02 m, multipath and noises are similar under open sky conditions, the system demonstrates a convergence time of less than 10 s. Moreover, the wide lane fixing rate is approximately 90%, while the narrow lane fixing rate can reach around 35%. The KPIs display greater sensitivity to satellite clock errors, followed by variations in tropospheric errors and satellite orbit errors. For instance, in the Gaussian model with 1000 runs at the 68th percentile, the difference between the minimum and maximum standard deviations scenarios for the satellite clock error group, troposphere group, and orbital error group is observed as 21 s, 5 s, and 1 s, respectively, in terms of convergence time. Noticeably, as the autocorrelation of errors increases from 0 to approximately 1, the convergence times at the 68th percentile in the "Baseßcenario exhibit values of approximately 13 s, 18 s, and 20 s for the three different conditions. The WL fixing rates for these conditions are 99%, 46%, and 43%, while the NL fixing rates are 38%, 15%, and 14%, respectively. Additionally, the average 2D position errors for the "Baseäre measured at 0.003 m, 0.012 m, and 0.015 m. In other words, in the AR model, an increase in the autocorrelation of errors is associated with a decline in KPIs performance. Additionally, variations in phase noise, spanning from 4 mm to 20 mm, exert an

impact on results. However, in scenarios with more lenient KPI criteria, this effect might be less conspicuous, potentially leading to a misguided assumption that it is inconsequential.

This work also presents suggestions for future investigations. Among them, there is the opportunity to improve the models to offer a more comprehensive framework suitable for various scenarios. Emphasis could be placed on refining the model's parameter selections through conventional computation or integration with AI technology, guided by long-term measurements. Furthermore, it is suggested to delve into the characteristics of other correction products that may potentially impact and degrade the performance of PPP.

Key words: Error Propagation, Convergence Time, PPP AR, Dual Frequency

Contents

List of Figures

List of Tables

Chapter 1

Introduction

1.1 Motivation and Objectives

GNSS enable autonomous positioning and timing data through constellations of satellites. Presently, four operational systems – namely, GPS of the United States, GLONASS of Russia, BeiDou of China, and Galileo of Europe – are evaluated based on four criteria: accuracy, integrity, continuity, and availability (European Union Agency for the Space Programme, 2023). The fundamental measurements for computing position and velocity, along with the receiver clock offset, include pseudorange, carrier-phase, and Doppler observations (Teunissen and Montenbruck, 2017). Undifferenced observation precision for phase is typically in the order of millimeters or even better, while the code measurement standard deviation can be less than 10 centimeters (Bona, 2000). High accuracy GNSS can be subdivided into two main methods: Real-Time Kinematic (RTK), which determines a position relative to a reference receiver and Precise Point Positioning (PPP), which estimates the absolute positioning using precise corrections generated by a network of reference stations (El-Mowafy, 2012).

RTK, known as one of the most precise positioning technologies, leverages carrier-phase measurements of satellite signals to provide users with centimeter-level position accuracy in real-time (Takasu and Yasuda, 2009). The standard mode for that involves placing one reference receiver at a station with coordinates known to very high precision while keeping the second receiver either static or moving within a close distance to the reference station (Rizos and Han, 2003). The basic concept is that, within a limited distance, the reference and rover experience the same or similar atmospheric delays, orbit errors, and satellite clock errors. By taking the double-differencing the measurements between the reference receiver and the user receiver, these effects can be mitigated or canceled out (Mageed, 2013).

However, the performance of positioning is constrained by the range between the users and the reference stations due to the spatial decorrelation of distance-dependent errors, such as ionosphere and troposphere errors (El-Mowafy, 2012). Additionally, the cost of the hardware, such as the firmware supporting RTK-GNSS on the receiver controller or PC, and the proprietary software remains high (Takasu and Yasuda, 2009). Furthermore, a major drawback of this method is that the rover's performance is highly sensitive to the corrections or measurements provided by the reference station (Mageed, 2013). Unreliable or mistaken information from the reference station can significantly compromise the integrity of the system. A technology is urgently needed to break the deadlock.

Shifting gears to the alternative method, PPP is a new category as absolute positioning, which represents a significant advancement in GNSS positioning and unrestrained solutions from the

erroneous fiducial constraints on any sites (Zumberge et al., 1997). Combining the strengths of GNSS standard single-point positioning (SPP) and GNSS relative positioning while mitigating their respective weaknesses, PPP is capable of processing static and kinematic data in both real-time and post-processing modes, provided that the corresponding product and calibration models are available. Importantly, PPP operates without the need for a reference station nearby, offering standalone operation, unconstrained by distance limitations, providing operational mobility and flexibility, and being cost-effective and computationally efficient (Choy et al., 2017).

Moreover, PPP allows for precise absolute positioning, directly determining station coordinates within the International Terrestrial Reference Frame (ITRF) (Zhang et al., 2017). The PPP approach is highly versatile and finds applications in various domains, including geodesy for tasks such as crustal deformation monitoring and the rapid processing of GNSS tracking station data. Additionally, it plays a pivotal role in diverse fields like agriculture, particularly in precision farming, marine surveys, and airborne mapping. Furthermore, it is instrumental in natural resource mapping and retrieval, precise time transfer, and atmospheric remote sensing, all representing active areas of application (Bisnath and Gao, 2009).

Nevertheless, limitations in ambiguity resolution, in convergence time as well as in accuracy restrict its further application (Wabbena et al., 2005). Residuals and noise persist in PPP calculations even after applying the correction service. Traditionally the correction products like satellite orbits and corresponding clock products are considered as deterministic values. However, it is important to acknowledge that in reality, these values are subject to certain uncertainties and inaccuracies (Odijk et al., 2014). Notably, even when utilizing the IGS's final product, the accuracies of correction products for GPS or GLONASS manifest in areas such as around 2.5 cm in orbit calculations, approximately 20 picoseconds in satellite correction products, and a 4 mm error in zenith troposphere delay (ZTD) (IGS, 2022). The current objective of PPP is to attain a synergy of high-precision localization and a substantial reduction in convergence time. This pursuit is paramount in the contemporary world, as its achievement would signify a profound transformation across various industries.

To delve deeper into this challenge, there is currently limited material to demonstrate that the initialization time of PPP can be reduced to well below several minutes. Highly precise ionosphere products may offer a solution to this issue (Choy et al., 2017). However, such precision in the ionosphere heavily relies on a dense network of reference stations, typically spaced tens of kilometers apart. Balancing the conservation of resources (ionosphere and dense reference network) while maximizing the performance of PPP has become a key focal point (Li et al., 2014b, Zhang et al., 2012). Reducing convergence time and refining kinematic applications could significantly enhance the practicality of PPP execution. The optimization of achieving consistent, robust, and economical positioning performance is imperative.

To achieve this goal, it is crucial to analyze the diverse error components that impact convergence time. By assessing the contributions of each component, we can prioritize areas for future improvement, concentrating on specific aspects that have a more significant influence on reducing convergence time. This targeted approach will guide our efforts towards achieving more efficient and faster PPP convergence. In addressing these challenges, our objective is to identify specific types of errors that, when subject to variation, significantly affect convergence time, fixing rate, and accuracy as key performance indicators (KPIs), with a particular emphasis on convergence time.

For the stated purpose, it is necessary to identify an appropriate model for expressing the behavior of correction product accuracies. The research conducted by Rankin (1994) simulated the pseudo-range errors and provided both Gaussian and Gaussian-Markov models. Inspired by this, and considering that the residuals have autocorrelations, two models are proposed to analyze the propagation of these residuals. The initial approach treats errors as a White Gaussian Noise process, while the subsequent method employs a first-order Auto-regressive model to simulate errors.

Still, it is crucial to acknowledge current limitations, encompassing time constraints and the scarcity of corresponding materials at our disposal. As a result, the focus of this study is primarily directed towards assessing the influence of error budgets, specifically stemming from correction product accuracies or uncertainties of satellite orbit errors, satellite clock discrepancies, and troposphere delay. Additionally, the models give precedence to errors from correction products manifesting on top of code measurements, with a simultaneous emphasis on ensuring that phase measurements remain within a predefined noise threshold. To align with real-world conditions, we introduce random noise to incorporate multipath and tracking noise on the code. To mitigate the interference of less relevant components and facilitate focused exploration of the errors under study, the magnitudes of multipath and tracking noises are intentionally constrained to a lesser extent. This approach creates what could be described as an "open sky" environment, ensuring that the primary emphasis remains on the errors being investigated.

1.2 Recent works on PPP techniques

Since the late 1990s, the concept of PPP has been developed to address the computational challenges posed by the rapidly increasing volume of data. This approach has been vigorously researched and studied at NASA's Jet Propulsion Laboratory (JPL) (Zumberge et al., 1997). This lead to significant advancements in the field. With the advancement of technology, the availability of real-time services provided by the International GNSS Service has become a reality. Pioneering studies employ the real time precise orbit and clock corrections to scrutinize the efficacy of PPP methodology. The outcomes of these investigations underscore the attainability of centimeter-level accuracy in position determination. Remarkably, convergence to such precision is achieved within just 20 min, thereby establishing PPP as a reliable and expeditious positioning technique (Chen et al., 2013, Gao and Chen, 2004). Real-time PPP results using the IGS Real-Time Service (RTS) products surpass the performance achieved with the ultra-rapid products. In fact, they exhibit an impressive improvement of approximately 50% when compared to the predicted satellite clock and orbit data provided by the IGS (Elsobeiey and Al-Harbi, 2016). In addition to research on the use of IGS data, a comprehensive exploration utilizing observational data from five Multi-GNSS Experiment (MGEX) stations is also analyzed. By employing the MGEX data, the static and kinematic modes are compared. Combining GPS with BDS outperforms GPS alone, with 57 min kinematic mode convergence and 50 min static mode convergence. In terms of positioning errors, they are within centimeter-level accuracy: 2 cm horizontally and 4 cm vertically in static mode and 3 cm horizontally and 9 cm vertically in kinematic mode (Xiong and Han, 2020). Further insights into PPP are explored by Chuanjuan, who delved into the performance of utilizing three constellations in PPP kinematic

mode. A proposed single and dual-frequency weighted combination method yielded a best-position 3D Root Mean Square (RMS) of 8.2 cm with a convergence time of 5.6 min (Zhang, 2020).

The trajectory of PPP research unfolds across several dimensions, notably encompassing PPP Ambiguity Resolution (PPP AR), PPP-Real-Time Kinematics (PPP-RTK), PPP-Inertial Navigation System (PPP-INS), and the integration of precise atmospheric models, where the latter can potentially improve the positioning performance by considering atmospheric such as corrections instead of estimated ones (Bisnath and Gao, 2009). The use of refined atmospheric models, confirmed by Cui et al. (2022), improves position accuracy and Time to First Fix (TTFF) in dual-frequency PPP methods.

The facts using real-valued float ambiguities experience long convergence times (Zumberge et al., 1997). This challenge prompts investigations into Ambiguity Resolution (AR) solutions, particularly in dual-frequency scenarios. Combining constellations in a dual-frequency, ionosphere-free situation becomes favorable. Notably, the use of GPS and GLONASS in PPP-AR method outperform the only GPS solution, drastically reducing initialization periods from over 25 min to around 6 min (Geng and Shi, 2017). In addition, the combination of GPS and Galileo also confirms the superior positioning precision compared to utilizing a single constellation only (Cui et al., 2022). The availability of multi-frequency GNSS observations also brings new perspectives. Within this context, the newer constellations BeiDou (BDS) and Galileo are gaining prominence. The triple frequencies combination within Galileo yields an averaged convergence time around 16.9 min while maintaining optimal positioning performance (Li et al., 2020). Based on triple-frequency, the fusion of BDS and Galileo enhances performance in terms of position accuracy and in both static and kinematic modes, compared to the ambiguity-float solution or dual-frequency scenario (Li et al., 2019). The performance of the triple-frequency combination is further supported by simulated data collected by Spirent, revealing both a high fixing rate and rapid convergence time (Liu et al., 2023b). In addition, multi-frequency has been used in the field of deformation monitoring. Application tests in deformation positioning using multi-frequency GNSS reveal that vibration frequency and amplitude can be accurately identified. However, the displacement derived from PPP AR remains noisier than that of RTK (Pan et al., 2023). It is worth noting that the PPP AR method alone may face challenges in ensuring high-speed convergence, especially after a receiver's cold start or any interruption in measurement due to signal obstruction (Choy et al., 2017).

PPP-RTK emerges as a synthesis, strategically combining the merits of conventional PPP and RTK methodologies. A pivotal distinction between PPP and PPP-RTK lies in the direct provision of atmospheric products, notably the ionosphere and troposphere, in the latter, as opposed to their frequencies combination or estimation in traditional PPP approaches (Wabbena et al., 2005). The undifered (UD) PPP-RTK method refines this concept through re-parameterized equations and processing at reference network stations. This intricate approach facilitates the derivation of network-based parameters, including satellite clock, phase biases, and interpolated atmospheric delay, which are then efficiently transmitted to end-users. Notably, empirical research attests to the efficacy of UD PPP-RTK, demonstrating its ability to swiftly resolve ambiguities and achieve high-precision positioning (Zhang et al., 2011). The inextricable linkage between ionosphere information and PPP-RTK performance propels ongoing research in the domain of ionosphere-constrained PPP-RTK. This focus is exemplified by investigations into the Time to First Fix (TTFF) for PPP-RTK constrained by the Global Ionosphere Map (PPP-RTK-GIM), which is reported to be approximately 8-10 min in this context. Furthermore, varying

TTFF values of 4.4 min, 5.2 min, and 6.8 min are observed when employing external iono-spheric information derived from different network scales (Zhang et al., 2022). However, the uniqueness of PPP as a global wide-area precision positioning technology would be greatly diminished if PPP is scaled down to require local/regional atmospheric corrections (Choy et al., 2017).

The challenges posed by unexpected observation discontinuity and unfavorable tracking geometry have led to the exploration of solutions aimed at enhancing the accuracy and reliability of the PPP method. In response, the integration of Inertial Navigation System (INS) terms with PPP has been proposed. Recent research focuses on tightly coupling multi-GNSS PPP with MEMS inertial measurement unit data, particularly in terms of position performance, resulting in significant improvements in accuracy and convergence time compared to relying solely on GNSS data but gains in velocity and attitude remain limited (Gao et al., 2017). The traditional PPP-INS system, utilizing a float solution for ambiguity, faces obstacles to widespread adoption. Ongoing investigations into ambiguity resolution methods seek to address this limitation. Studies, such as those by (Liu et al., 2016), reveal that the overall performance of PPP-INS systems can be comparable to that of Differential GNSS (DGNSS)/INS systems, achieving centimeter-level position accuracy and rapid convergence time. Consequently, PPP-INS emerges as a potential solution to meet the escalating demand in the automated car navigation field, offering sub-meter level accuracy at the lowest possible cost. Empirical evidence in open-sky and suburban environments substantiates its performance (Elsheikh et al., 2019).

This thesis comprises six chapters. Beginning with the introduction, we delve into error budgets associated with GNSS positioning. Advancing from there, we investigate observation equations and their combinations, along with a detailed exploration of the architecture of the PPP-AR engine employed in our analysis. Subsequently, we provide insights into the simulation setup and the sensitivity approach employed. Finally, we present and discuss the outcomes, concluding with a summary of findings and directions for future research stemming from this investigation. This structured approach enhances the coherence between paragraphs, ensuring a seamless flow of information throughout the thesis.

Chapter 2

Principles of Positioning

Conventionally, raw phase measurements (L) and code measurements (P) on frequency i ($i = 1, 2$) from receiver r to satellite s are denoted as follows (Liu et al., 2023a):

$$L^s_{r,i} = \rho^s_r + c(dt_r - dt^s) - \gamma_i I^s_{r,1} + M^s_r T_r + \lambda_i(N^s_{r,i} + B_{r,i} - B^s_i) + \epsilon L_i \quad (2.0.1)$$

$$P^s_{r,i} = \rho^s_r + c(dt_r - dt^s) + \gamma_i I^s_{r,1} + M^s_r T_r + b_{r,i} - b^s_i + \epsilon P_i \quad (2.0.2)$$

Where:

- ρ^s_r indicates the geometric distance,

- dt_r and dt^s denote the receiver clock and satellite clock offset,

- c : the speed of the light,

- $\gamma_i = \frac{f^2_1}{f^2_2}$: transformation factor for converting ionospheric effects from carrier phase L1 frequency to Li frequency,

- $I^s_{r,1}$: first-order ionospheric influence on the frequency L1,

- M^s_r : mapping function of troposphere,

- T_r : zenith troposphere delay,

- λ_i : carrier phase wavelength,

- $N^s_{r,i}$: the integer ambiguity on frequency i,

- $B_{r,i}, B^s_i$: the receiver-dependent and satellite-dependent phase biases,

- $b_{r,i}, b^s_i$: the hardware code bias originated from receiver and satellite,

- $\epsilon L_i, \epsilon P_i$: other error terms, such as measurement noise, thermal noise and multipath, etc.

Measurement errors encompass a variety of factors, including satellite orbit errors, satellite clock errors, signal propagation through the atmosphere, as well as phase and code biases originating from both satellites and receivers. Additionally, errors can arise from receiver noise, multipath interference, and other factors like phase wind-up and in static mode, site displacement effects. Given that the PPP method demands precise correction products to mitigate errors effectively, comprehending the nature of these errors and employing appropriate strategies is crucial for optimizing its performance.

It is evident that ionospheric delays affect phase and code measurements to the same extent but with opposite signs. This is due to the inherent properties of the ionospheric layer and the

signals as electromagnetic waves; this can lead to phases and groups having different velocities. In other words, two different refractive indexes can be defined for the group and phase. Details can be found in Section 2.2. In addition, multipath and noise are significant sources of error under critical surrounding observing conditions. The presence of phase biases also affects the integer characteristics of ambiguities if not addressed effectively.

2.1 Satellite Orbit and Clock Errors

Satellite-based orbit and clock errors are crucial factors in the field of precise positioning. This is why they receive significant attention, e.g., with a dedicated portion of the IGS established to furnish precise orbit and clock information.

2.1.1 Satellite Orbit Errors

Orbital errors occur because of the discrepancies from a satellite being in a different location from its real location (Ogaja). In the field of precise point positioning, the accuracy of satellite orbits affects the positioning performance directly. Although Kepler's laws elegantly describe the motion of satellites in terms of the ideal situation in which the Earth is considered to be a point mass or a spherically symmetric mass distribution, in reality, the Earth exhibits a complex and inhomogeneous shape and mass distribution, which prevents these ideal orbits from accurately reflecting the actual motion of satellites. In addition, disturbing forces from celestial bodies such as the Moon and the Sun also have a significant impact on satellite orbits. Gravitational perturbations from the Moon and the Sun, coupled with the effects of tidal deformation, further increase the challenge of establishing precise orbits. In addition to gravitational perturbations, factors such as radiation pressure and atmospheric drag introduce complexities that make it even more challenging to achieve high-precision satellite orbits (Teunissen and Montenbruck, 2017).

The high precision demands of the PPP method for the correction products necessitate for the pursuit of more precise orbits. Consequently, the active engagement of both commercial and complementary organizations becomes essential, necessitating supplementary calculations to derive orbits with enhanced precision. The products available through the IGS platform have resulted in considerable accuracy and homogeneity of GPS satellite orbits. Within the IGS repository, users can access an array of orbit products, including ultra-rapid, rapid, and final solutions (IGS, 2022). The IGS final products result from the collaboration of several IGS Analysis Centers (ACs) utilizing six largely independent software packages (e.g., BERNESE, GAMIT, GIPSY, NAPEOS, EPOS, and PAGES) (Kouba, 2009). Due to varying accuracy requirements, the processing conditions may undergo specific adjustments, influencing the production of rapid products, for example. There are differences in the tracking data obtained from different stations within the IGS global tracking network due to differences in acquisition methods, communication schemes and levels of quality control. Together, these differences contribute to the latency problem (Kouba, 2009). The assessment of orbital accuracy is typically quantified by calculating the one-dimensional root-mean-square (RMS) values of the three geocentric XYZ components. It is worth noting that the highest achievable accuracy is currently about 2.5 cm with a latency of 12-18 days (Teunissen and Montenbruck, 2017). The ultra-rapid (half the prediction) products achieve commendable accuracy, typically reaching a critical value of 5 cm,

but have somewhat less latency. It is crucial to highlight that a trade-off exists between latency and accuracy; products with reduced latency tend to exhibit diminished accuracy.

2.1.2 Satellite Clock Errors

Satellite clock instabilities are another error source that affects the positioning performance. When satellites use rubidium and cesium atomic standards, they are subject to clock noise and frequency variations that are varied and therefore difficult to predict (Hauschild and Montenbruck, 2009). Various methods can be used to mitigate or minimize the clock errors. One such method is to utilize the parameters in the satellite ephemeris broadcast messages when ultra-high accuracy is not strictly required. Alternatively, a differential method can be used, whereby one satellite is observed through two receivers.

These clock errors can be divided into two different types: physical synchronization errors and mathematical synchronization errors. The former refers to the difference between the satellite clock and the standard time. At the same time, the latter arises from errors introduced when using polynomial coefficients and is characterized by inaccuracies in the clock parameters (offset, variation, and variation rate) as well as random errors embedded in the equations.

High-precision clock products are typically spaced in intervals of minutes or tens of seconds, so the need for linear interpolation depends on the individual projects (Elsheikh et al., 2023). The IGS product is an exceptionally precise resource typically used in the PPP method with considerable accuracy. The accuracy of the final product is at its peak in the IGS service product range, with line-of-sight deviations consistently approximately 0.006 m. Notably, IGS products were initially focused solely on the GPS and a substantial quantity of GLONASS. The emergence of the IGS Multi-Global Navigation Satellite System Experiment (MGEX) project compensated for the shortcomings of the IGS by providing products for all GNSS constellations (Montenbruck et al., 2014).

2.2 Ionospheric Delays

GNSS signals traverse the Earth's atmosphere, first encountering the ionosphere layer at altitudes ranging from 50 to 1000 km above the Earth's surface. This region is significantly influenced by solar activity, leading to the generation of free electrons. These electrons, in turn, introduce deviations in the curvature of signal paths and variations in the speed of radio waves compared to their propagation in the vacuum of space. Notably, the ionosphere is a dynamic layer subject to constant change, influenced by alterations in the Earth's rotation. This dynamic nature adds complexity to the behavior of GNSS signals within the ionosphere. The velocity V_p inside the ionosphere layer can be expressed as follows:

$$V_p = \frac{c}{n_p} \tag{2.2.1}$$

where c is the speed of light in vacuum, n_p is a refractive index. The refractive index is unitless and it depends on the frequency. This refractive index can be further explained by the following simplified function (Teunissen and Montenbruck, 2017):

$$n_p = 1 \pm \frac{40.3 n_e}{f^2} \tag{2.2.2}$$

where n_e is the electrons density, and its unit is given in electrons per meter cubic (e^- / m^3). f is the frequency of the signal. From the above, the ionospheric effect depends only on these two factors. We use the total electron Content (TEC) to replace n_e for ease of calculation. The behavior of radio waves in the ionosphere is proportional to TEC, which varies with location, time of day, season, and solar activity. After organizing these functions, the ionospheric delay can finally be expressed as:

$$\Delta L = \pm \frac{40.3 \, \text{TEC}}{f^2} \tag{2.2.3}$$

It is notable that the pseudorange experiences a delay, while the phase experiences an advance of the same magnitude.

Correct handling of ionospheric delays contributes to better performance positioning. There are two fundamental approaches in ionospheric delay calibration: 1) modeling methodologies and 2) dual-frequency combinations. Both contribute to mitigating or minimizing their impact. The former encompasses empirical modeling and accurate measurement modeling, which previously relies heavily on such as interpolation techniques and the Klobuchar model method when only a single signal is available. In addition, these methods may not meet the stringent accuracy requirements of some users, especially since empirical modeling tends to produce less accurate results. As technology advances, the emergence of dual-frequency solutions offers a new avenue. The ionosphere-free linear combination can be seen as follows:

$$L_{IF} = \frac{f_{L1}^2}{f_{L1}^2 - f_{L2}^2} L_1 - \frac{f_{L2}^2}{f_{L1}^2 - f_{L2}^2} L_2 \tag{2.2.4}$$

Where the new observation L_{IF} cancels the first-order ionospheric delay.

2.3 Tropospheric Delays

The troposphere, extending from the Earth's surface to an altitude of about 10 kilometers, plays a vital role in the propagation of radio waves. In this layer, the speed of radio waves undergoes changes, deviating from the speed of light. While refractive effects are present within the troposphere, applying a dual-frequency correction, similar to the ionospheric correction, proves challenging. This difficulty arises because the high frequency of radio waves has minimal impact on different carriers compared to signals in the ionosphere layer. However, the GNSS signal propagation is decelerated due to its refractive properties. This deceleration is not only inversely proportional to the speed of the radio waves but also depends on the observatory condition's, including temperature, pressure, and humidity aspects. Modern modeling techniques have become very proficient in the hydrostatic domain. However, the estimation of the wet part of the tropospheric delay is still remaining as a formidable challenge.

Many scientific publications have meticulously researched and dissected the methods of calibrating tropospheric models, reflecting the relentless efforts to improve the accuracy and understanding of these intricate atmospheric processes. Well-known models, such as Hopfield and Saastamoinen, have proven effective under drought conditions (Hopfield, 1963, Saastamoinen, 1972). However, potential errors may arise due to flaws in the models themselves. Due to the deviation of the actual weather conditions from the one deducted by empirical model parameters, the values of the tropospheric delay would differ from the actual delay. Moreover, inaccuracies in tropospheric corrections can come from several sources, including instrumental differences, inaccurate readings, and local temperature differences. Careful consideration of these variables is necessary when dealing with tropospheric correction procedures.

Typically, in the delay section, the computation starts with the zenith delay, which is then enriched to approximate reality using a mapping function. The zenith delay is further divided into the Zenith Hydrostatic delay (ZHD) and the wet component (ZWD). For the ZHD, Saastamoinen's model is commonly employed, providing a foundation for accurate calculations in the hydrostatic domain. This model's formula is given as follows (Saastamoinen, 1972):

$$Z_h = \frac{0.0022768P}{1 - 0.00266\cos(2\phi) - 2.8 \times 10^{-7}h} \tag{2.3.1}$$

where, P is the surface pressure, which can be computed approximately from the function provided by Berg (1948), ϕ represents the latitude, and h denotes the height. The ZHD from 2.3.1 is precise enough while the ZWD can only get the initial values from it and further estimated by the navigation filtering process (Elsheikh et al., 2023).

For the mapping functions, the most primitive and fundamental equation is given by Marini (1972):

$$M(e) = \frac{1 + \frac{a}{1 + \frac{b}{1+c}}}{\sin e + \frac{a}{\sin e + \frac{b}{\sin e + c}}} \tag{2.3.2}$$

where, e is the satellite's elevation angle, and a, b, c are constant coefficients, which are much less than 1 and can be found from the paper proposed by Davis et al. (1985).

All the existing mapping functions are derived from the above equation (Elsheikh et al., 2023). The widely used combination of mapping functions consists of two empirical models: the Global Pressure and Temperature (GPT) model and the Global Mapping Function (GMF) model. As its name suggested, the former provides information on pressure and temperature, while the latter gives the final mapping function based on the provided GPT information. Still, they are constrained by the spatial and temporal variability. To address these limitations, a new combined model, GPT2, has been introduced to yield solutions to overcome the limitations as mentioned above. GPT2 offers the pressure, temperature, lapse rate, water vapor pressure, and mapping function coefficients at any site, resting upon a global $5°$ grid of mean values, annual, and semi-annual variations in all parameters (Lagler et al., 2013).

2.4 Receiver Noise and Multipath

Imperfections in various electrical components within the signal processing chain and the interference caused by natural or artificial sources in the environment contribute to measure-

ment noises (Hauschild, 2017). There are random errors present in both the code and carrier phase measurements. The width of the correlation function serves as one of the contributing sources. In general, the receiver noise error is around 1% of the wavelength of the signal involved (Hebert, 1995). This implies that for the GPS C/A code, there can be up to 3 m of noise, whereas the L1 frequency is affected by only a few millimeters.

Multipath is a major source of error in positioning. Thus, understanding the effects of multipath is essential for GNSS positioning. In the presence of multipath effects, the receiver captures a combination of both direct and reflected signals. In situations where multipath interference is absent, carrier phase measurements can be made with high accuracy, with noise on the order of millimeters. Similarly, code measurements are accurate to the order of decimeters. This accuracy is crucial for PPP. However, the occurrence of multipath interference can disrupt these precise measurements and introduce errors into the positioning system. A maximum value of a quarter of a cycle can appear in the phase measurement, while pseudorange multipath can extend up to hundreds of meters for C/A-code measurements (El-Rabbany, 2002).

Several indices can be used to characterize multipath effects. One such index is the "path difference," which indicates the difference between the direct and reflected signal paths. By the ratio of this difference to the signal's wavelength, we can determine the "phase difference." In addition, the reflection index helps us understand the reflection's strength. For example, the reflection coefficient (e.g., of a water surface) can be 1, which means that the signal is completely reflected without any loss of signal power, which can be fatal to the measurement. However, in most cases, signals from reflected paths experience signal power loss, phase delay, and polarization changes. Accurately quantifying multipath effects is challenging due to the complexity of multipath signal geometries and the challenge of determining reflection indices (e.g., point of reflection and degree of reflection). In addition, different receiving stations are affected differently by multipath interference. Therefore, using mathematical models to eliminate multipath errors is complex, and even inter-site differencing techniques cannot fully mitigate multipath effects.

Still, there are some strategies to minimize multipath interference. First, avoid highly reflective surfaces such as lakes or nearby walls when choosing a receiver location. Second, specialized antenna designs with anti-multipath features can help reduce the reception of reflected signals. In addition, specific software tools can help mitigate the multipath effect. However, the most effective method is to avoid multipath (Yedukondalu et al., 2011).

2.5 Phase and Code Biases

The phase and code biases stem from imperfections in the hardware used in the satellites and receivers. As a result, there is still a time delay from driving the clock that generates the signal to the antenna transmitting the signal. Better estimation or correction of them could improve the performance of the PPP method. Therefore, it becomes crucial to identify these biases.

Proper handling of code biases is indispensable. Regarding two types of code biases, the receiver bias and satellite-based bias are usually considered independent of each other. The receiver bias is commonly lumped with the estimated receiver clock bias (Elsheikh et al., 2023). The satellite-based part can be processed by introducing the differential form, Differential Code Bias (DCB), where DCB represents the time delay between two code observations of the same

satellite at the same or different frequency (Montenbruck and Hauschild, 2013). Organizations such as IGS can provide it or from real-time through the IGS RTS or by considering the corresponding parameters from the navigation message. There are several types of parameters available, such as the Timing Group Delay (TGD) and the Inter-Signal Correction (ISC) parameters. Additionally, the Inter-System Bias (ISB) is released to deal with the delays between the GNSS systems. The typical approach estimates its values for each constellation as a time offset relative to GPS. Notably, the GLONASS satellite code biases should be considered carefully due to the Frequency Multiple Access Devision (FDMA). Thus, the Inter-Frequency Bias (IFB) is introduced. In conclusion, as mentioned earlier, correctly utilizing the products is vital.

Phase biases are categorized into receiver bias and satellite-dependent bias. Their characterization prevents the correctness of ambiguity integer features in the calculation. For the relative positioning approach like RTK, they are canceled out by double differences of observations. As for the PPP method, typically, a single difference between satellites helps to eliminate receiver-dependent phase bias. For the case where the PPP methods use floating solutions, the phase bias is superimposed on the floating ambiguity in the filtering. For integer fixed PPP solutions, there are efforts to use phase bias correction values computed from a global or regional reference station network, and it is pretty significant (Hauschild, 2017). An alternative is the reparameterization of bias in order to recover the integer nature of the ambiguity (Liu et al., 2023a).

2.6 Antenna Phase-Center Offset and Variations

Two types of effects concerning the antenna phase center are Phase Center Offset (PCO) and Phase Center Variation (PCV). PCO refers to the offset between the average phase center locations relative to a physical reference point (Cisak and Zanimonskiy, 2008). In reality, the GNSS antenna phase center varies in time. PCV is the deviation of the actual phase center from the mean antenna phase center (EL-Hattab, 2013). The occurrence of those errors related to the satellites is because precise satellite data such as the IGS $SP3$ files are typically referred to the Center of Mass (CoM) instead of Antenna Phase Centers (APCs), used in the actual measurement. If there are no corrections, for receiver antennas, the magnitude of PCO can be around 5 to 15 cm while the PCV can be 3 cm while for satellite, the PCO is between 0.5 and 5 cm (Elsheikh et al., 2023). Therefore, it must be addressed in the field of precise positioning.

Fortunately, calibration tables for the absolute antenna Phase Center Variations are accessible on the IGS website through the ANTenna Exchange (ANTEX) file. Attention should be given to corrections for both receiver and satellite antennas to ensure consistency. For instance, the inconsistent application of the absolute and relative or no PCVs from the receiver and satellite antennas may lead to decimeter solution errors (Teunissen and Montenbruck, 2017).

2.7 Relativistic Effects

Due to the distinct environments of clocks on the ground and satellites, various relativistic effects, including both special and general relativity, come into play. General relativity occurs because the Earth's gravity affects the two clocks on the satellite and on the ground differently. In contrast, special relativity is induced by the difference in speed between them (Hećimović,

2013). Although the impacts of special relativity are relatively minor, those of general relativity are significantly more pronounced. Typically, relativistic effects are considered during satellite manufacturing, leading to a slightly slowing down of the clock frequency from real-time. Ground-based clocks also need to account for the effects of special relativity, but given the lower relative speeds, this effect is automatically factored into the receiver's clock difference.

2.8 Others

For precise positioning, further consideration needs to be given to error terms such as site displacement effects and phase wind-up errors. Within the site displacement effects, the largest errors are usually due to solid Earth tides and oceanic loads caused by the Earth's gravitational pull exerted by the Sun and Moon.

Chapter 3

Precise Point Positioning

3.1 PPP Concept Overview

PPP has been proven as a potentially powerful tool in geodetic and geodynamic-related activities since it allows users to ignore the covariances among different stations, which hugely reduces the computation burdens (Ge et al., 2008). Typically, precise orbit products and satellite clock corrections are utilized, along with correction products such as troposphere delays, PCO, PCV, relativity effect, etc. After applying all the corrections, the residuals are reduced. Additionally, precise phase measurements are achieved with millimeter-level noise, and code measurements have noise at the sub-meter or centimeter-level.

When discussing PPP, achieving highly accurate positions is feasible, provided that convergence has occurred. However, a well-known challenge lies in the convergence time, particularly for users requiring rapid position determination. To address the need for both high precision and minimal waiting time, various techniques have been developed. For instance, PPP-RTK integrates conventional PPP with corrections from RTK networks, such as troposphere and ionosphere corrections. Another approach is PPP-INS, which leverages the continuous position updates offered by combining PPP with INS. This method relies on the acceleration and gyroscope data from the INS to continuously track changes in velocity and orientation, providing accurate positioning.

Alternatively, PPP AR employs algorithms like the Least-squares Ambiguity Decorrelation Adjustment (LAMBDA) method, proposed by Teunnissen (1995) or the modified Least-squares Ambiguity Decorrelation Adjustment (mLAMBDA) (Chang et al., 2005). After obtaining a float solution through filtering, these algorithms assist in determining integer values for ambiguities without the need for external aids like RTK products or INS. Resolving ambiguities efficiently results in quick and precise positioning outcomes. In our study, we aim to explore scenarios where limited data is available, yet users can still derive benefits from the PPP method. This motivation underlies our focus on analyzing the error behaviors within the PPP AR framework.

Measurements typically contain errors even after applying correction products. Common approaches involve using differences between measurements or combining them, aiming to obtain less noisy results and facilitating subsequent processing. The wavelengths of L1 or L2 frequencies, such as approximately 20 cm for GPS L1, pose a challenge when determining ambiguity. Noisy measurements complicate the ambiguity resolution process. To address this challenge, a way known as combination involves both Wide Lane (WL) and Narrow Lane (NL) combinations. WL combination adjusts coefficients of measurements to increase the combined

wavelength, for example, to around 86 cm, making it easier to resolve. However, this amplifies noise due to the addition of code measurements and the new formation function. Additionally, WL combination results in the loss of location information, disconnecting it from specific positions. To overcome this limitation, NL is introduced. By combining measurements, the wavelength becomes smaller, but improving noise characteristics. Combining both WL and NL benefits allows for mitigating their respective drawbacks. For instance, the fixied WL ambiguity from the WL combination process helps quick resolve the NL ambiguity while NL gives less noisy measurement and position information (Li et al., 2014a). This combined approach is commonly employed in the field of PPP.

The Kalman filter is adept at updating its estimates based on new measurements, making it particularly suitable for real-world applications where situations may vary. Its recursive nature allows it to excel in dynamic systems, providing real-time state estimates. Moreover, the Kalman filter demonstrates resilience in handling noisy measurements, minimizing the impact of highly noisy measurements on the final results. This resilience is achieved through the Kalman gain, a mechanism that adjusts the weighting of measurements. The filter assigns more weight to measurements with lower uncertainty while assigning smaller weight to noisy measurements (Teunissen and Montenbruck, 2017). As a result, the Kalman filter effectively mitigates the influence of highly noisy measurements, contributing to more robust and accurate state estimates. These characteristics make the Kalman filter highly favorable. In our study, we employ the Kalman filter as a filtering method.

In general, in our PPP AR approach, the raw data is error-free simulated data. We employ error simulation models to replicate errors, mimicking the raw measurements obtained from a real receiver. For more detailed explanations, please refer to Chapter 4. The dual-frequency ionosphere-free (IF) model is employed in both WL and NL combinations to eliminate the influence of the first-order ionospheric delays. A popular method in the WL ambiguity generation process is the method - Melbourne and Wübbena (MW) combination (Blewitt, 1990). This approach offers the advantage of canceling out the ionospheric effects and yielding a larger wavelength. The ambiguity resolution status in the WL phase is a crucial determinant, indicating whether a pure ionosphere-free combination or the NL combination is selected for the subsequent filtering method. Due to the nonlinearity of functions, such as position in relation to the range or pseudorange, a crucial step before subsequent processes involves linearization. This is achieved through techniques like Taylor expansion.

Consequently, two types of ambiguities exist in the results of the Kalman filter method. Only when the WL ambiguities are successfully resolved will the corresponding NL ambiguities proceed into the mLAMBDA process, which directly impacts position solutions. During the mLAMBDA process, decisions are made to either fix or maintain float ambiguities, and two tests are employed for this purpose: the ratio test and the residual test. While the ratio test is a common practice in the LAMBDA method, the residual test is a novel addition, aligning with its effectiveness, especially evident in our simulated data. If certain ambiguities are resolved, position solutions are updated, incorporating the contributions of the fixed ambiguities. In the subsequent epoch, the resolved ambiguity is preserved, and these values serve as the initial values for the next epoch. The entire process concludes when the selected measurement epochs reach their conclusion. This procedural flow is illustrated in Figure 3.1, providing a visual representation of the methodology employed in our study. The upcoming sections delve into more in-depth details, offering insights into the mathematical perspective of those combinations, the involved functions, and the specific values within the Kalman filter.
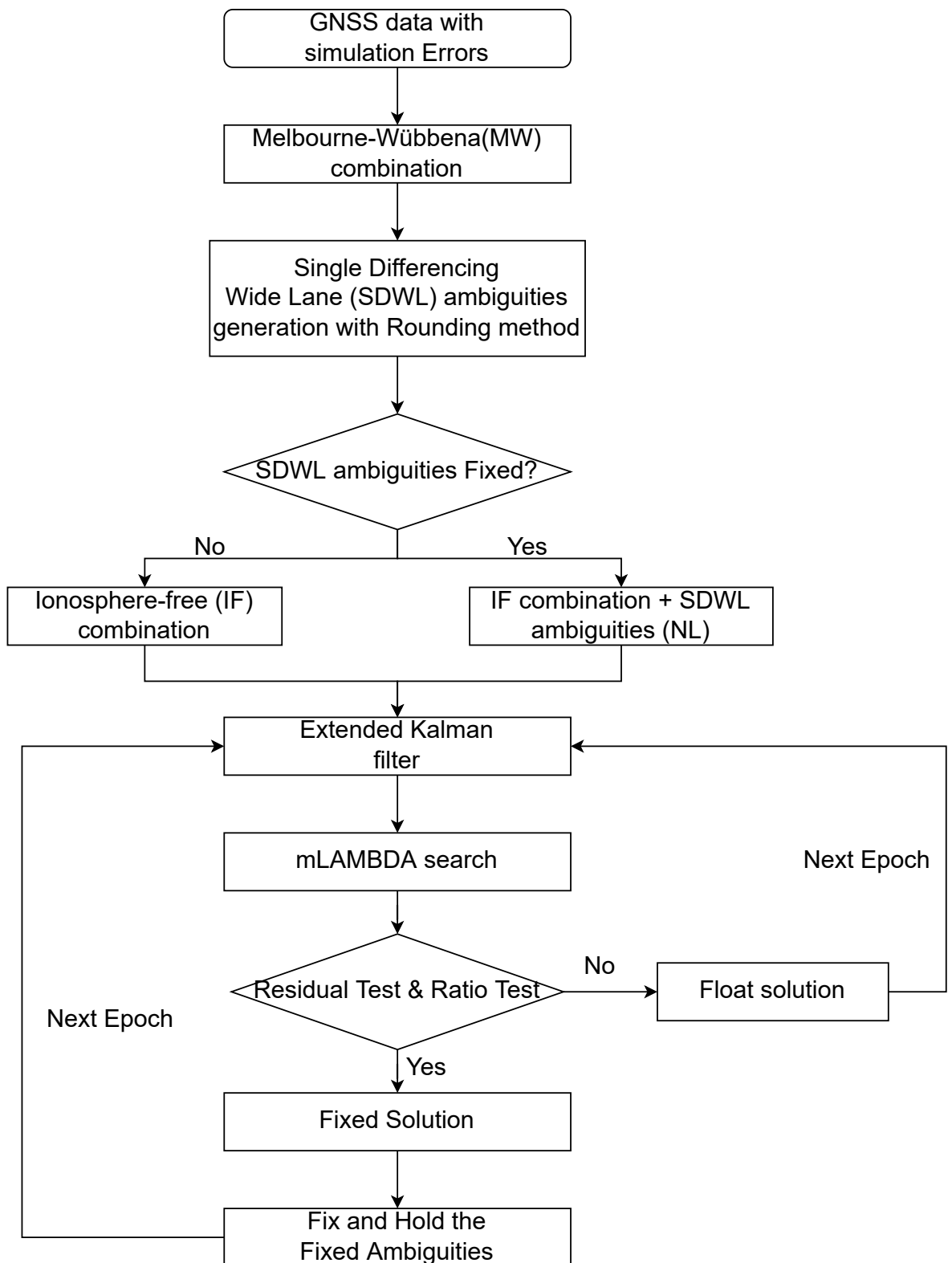
Figure 3.1: *Flowchart of Depicting the Filtering steps in the PPP AR Engine*

3.2 Single Differencing Wide Lane Combination

According to the proposal of Melbourne and Wübbena, the MW combination is used as the WL combination in which ionospheric delays, clocks, and non-dispersive delays are effectively canceled (Li et al., 2014a). The MW combination is a bridge to solve the ambiguity problem. In other words, it is a geometry-free model, and it eliminates the first-order effects of the ionosphere. Geometry-free implies the elimination of the geometric component in the measurement, retaining only the frequency-dependent effects such as ionospheric refraction, instrumental delays, wind-up, in addition to multipath and measurement noise in practice. The MW combination provides additional information for ambiguity determination but does not directly contribute to the position determination process.

The equations can be formulated as follows:

$$L^s_{r,WL} \quad = \quad \frac{f_1}{f_1 - f_2} L^s_{r,1} - \frac{f_2}{f_1 - f_2} L^s_{r,2} \tag{3.2.1}$$

$$P^s_{r,WL} \quad = \quad \frac{f_1}{f_1 + f_2} P^s_{r,1} + \frac{f_2}{f_1 + f_2} P^s_{r,2} \tag{3.2.2}$$

By subtracting 3.2.1 and 3.2.2, then we get MW equation:

$$
\begin{aligned}
MW_s \quad &= \quad L^s_{r,WL} - P^s_{r,WL} \\
&= \quad \lambda_{WL}(N^s_{WL}) + \Phi^s_{WL} + \epsilon^s_{WL}
\end{aligned}
\tag{3.2.3}
$$

Where N^s_{WL} is the WL ambiguity, ϵ^s_{WL} is the noise and other error terms after MW combination. ϕ^s_{WL} refers to the biases; here, we assume that the satellite and receiver-related hardware delay are fully corrected, which means it is equal to 0. And λ_{WL} is the WL wavelength, which is around 1.01 m for Galileo and 0.86 m for GPS. This gives the advantage to fix the ambiguity easily. The WL ambiguity is defined as $N^s_{WL} = N^s_1 - N^s_2$.

Single differencing between satellites or receivers, as well as double differencing, are methods for eliminating or reducing errors in GNSS positioning. Single differencing between satellites works effectively for correcting receiver clock errors and initial receiver-dependent biases, while single differencing between receivers can reduce satellite clock errors and their corresponding biases. In the PPP method, single differencing between satellites is the only option. This helps cancel out the impact of receiver hardware delays. We select a reference satellite for each satellite constellation, denoted by the superscript *ref*. By performing single differencing between a satellite and its respective reference satellite, we obtain a new ambiguity term denoted as:

$$N^{s,ref}_{WL} = N^s_1 - N^s_2 - (N^{ref}_1 - N^{ref}_2) \tag{3.2.4}$$

Rounding the WL ambiguity and comparing its value with threshold settings helps decide whether the WL ambiguity should be treated as a float or fixed. The resolution status of the Wide-Lane ambiguity determines the observation combinations utilized as input for the Extended Kalman Filter process.

3.3 Single Differencing Narrow Lane Combination

This procedure serves as the input for the observation part. For the code measurement, a dual-frequency geometry-based ionosphere-free combination is applied:

$$P^s_{r,NL} \quad = \quad \frac{f_1^2}{f_1^2 - f_2^2} P^s_{r,1} - \frac{f_2^2}{f_1^2 - f_2^2} P^s_{r,2} \tag{3.3.1}$$

For the carrier phase measurement, two combinations are employed based on the condition of the SDWL ambiguity. If the SDWL ambiguity is a float value, the conventional ionosphere-free combination is taken as follows:

$$L^s_{r,NL} \quad = \quad \frac{f_1^2}{f_1^2 - f_2^2} L^s_{r,1} - \frac{f_2^2}{f_1^2 - f_2^2} L^s_{r,2} \tag{3.3.2}$$

If the SDWL ambiguity is fixed, then we will take advantage of the benefits of the wide-lane results. Additionally, there will be a special step later on for the float ambiguities generated by the Kalman filter using the NL combination. These float ambiguities will be fed into the mLAMBDA to attempt fixing them. The equation would be:

$$L^s_{r,NL} \quad = \quad \frac{f_1^2}{f_1^2 - f_2^2} L^s_{r,1} - \frac{f_2^2}{f_1^2 - f_2^2} L^s_{r,2} - \frac{\lambda_2 f_2^2}{f_1^2 - f_2^2} N^{s,ref}_{WL} \tag{3.3.3}$$

By reorganising, the above equation 3.3.3 can be formed as below:

$$L^s_{r,NL} \quad = \quad \rho^s_r + \lambda_{NL} \Delta N^{s,ref}_{r,1} + \lambda_{IF} N^{ref}_{IF} + \epsilon_{L^s_{r,NL}} \tag{3.3.4}$$

Where λ_{NL} is defined as $\frac{c}{f_1 + f_2}$, where c is the speed of light and f_1 and f_2 are the frequencies. The subscript IF denotes the ionosphere-free combination. Only the ambiguity difference between a satellite and its reference satellite is considered in the mLAMBDA process. The ambiguity denoted by the IF part remains as a float.

3.4 Least Square Estimation with Weight Constrains

In most cases, the initial values are usually unknown. The Least Squares (LS) method is used to provide the initial position and other relevant parameter values as well as corresponding initial covariance for later filtering methods. Doppler measurements yield lower noise than code measurements under critical conditions, such as frequent carrier phase outages, making them a favorable choice (Li et al., 2011). Within the precise point positioning method, both Doppler measurements on f_1 frequency and dual-frequency ionosphere-free pseudorange combinations are employed in computations. After applying the first-order Taylor expansion to linearize, the equations take the following form:

$$P^s_{IF} = \frac{x_r - x_s}{\rho^s_r} dx_r + \frac{y_r - y_s}{\rho^s_r} dy_r + \frac{z_r - z_s}{\rho^s_r} dz_r + d(c\hat{t}_r) + dTro^s + \epsilon P^s_i + P^0_{IF} \tag{3.4.1}$$

$$f^s_{di} = \frac{1}{\lambda} \left(\frac{v_{x_s} - v_{x_r}}{\rho^s_r} + \frac{x_s - x_r}{(\rho^s_r)^3} \right) dx_r + \frac{1}{\lambda} \left(\frac{v_{y_s} - v_{y_r}}{\rho^s_r} + \frac{y_s - y_r}{(\rho^s_r)^3} \right) dy_r +$$

$$\frac{1}{\lambda} \left(\frac{v_{z_s} - v_{z_r}}{\rho^s_r} + \frac{z_s - z_r}{(\rho^s_r)^3} \right) dz_r + \frac{1}{\lambda} \left(\frac{y_r - y_s}{\rho^s_r} dx_r + \frac{y_r - y_s}{\rho^s_r} dy_r + \frac{z_r - z_s}{\rho^s_r} dz_r \right) + \epsilon f^s_{di} + f^0_{di}$$

$$\tag{3.4.2}$$

In the context of our notation, the lowercase variables x, y, and z signify the three spatial directions of position. The symbol ϵ is employed to denote the noise associated with both code and Doppler measurements, with the superscript "0" indicating an approximate measurement. The symbol r is utilized to represent receiver-dependent variables. Meanwhile, s denotes the satellite number, and f_{di}^s specifically refers to the carrier Doppler measurement associated with satellite s. The wavelength of the satellite signal is denoted by the symbol λ. Since The above equations can be written as follows:

$$V = Ax + e \tag{3.4.3}$$

where A refers the design matrix, the unknown vector is corrected by the unknown term $\hat{x}$, and V is used as residual vector.

The unknown matrix consists of position in x z y directions, the receiver clock offset errors, as well as their corresponding velocities, the troposphere error terms and the inter constellation time differences, here is between GPS:

$$x = \begin{bmatrix} dx \\ dy \\ dz \\ d(cdt_r) \\ d\dot{x} \\ d\dot{y} \\ d\dot{z} \\ d(cd\dot{t}_r) \\ dTro^s \\ dT_{sys} \end{bmatrix} \tag{3.4.4}$$

where the last term dT_{sys} is the system time difference between the Galileo and the GPS. The design matrix is:

$$A = \begin{bmatrix} \frac{x_r-x_1}{\rho_r^s} & \frac{y_r-y_1}{\rho_r^s} & \frac{z_r-z_1}{\rho_r^s} & 1 & 0 & 0 & 0 & 0 & M_r^1(\theta) & 0 \\ \frac{x_r-x_2}{\rho_r^s} & \frac{y_r-y_2}{\rho_r^s} & \frac{z_r-z_2}{\rho_r^s} & 1 & 0 & 0 & 0 & 0 & M_r^2(\theta) & 0 \\ \vdots & \vdots & \vdots & \vdots & \vdots & \vdots & \vdots & \vdots & \vdots \\ \frac{x_r-x_s}{\rho_r^s} & \frac{y_r-y_s}{\rho_r^s} & \frac{z_r-z_s}{\rho_r^s} & 1 & 0 & 0 & 0 & 0 & M_r^s(\theta) & 1 \\ 0 & 0 & 0 & 0 & \frac{x_r-x_1}{\rho_r^s} & \frac{y_r-y_1}{\rho_r^s} & \frac{z_r-z_1}{\rho_r^s} & 1 & 0 & 1 \\ 0 & 0 & 0 & 0 & \frac{x_r-x_2}{\rho_r^s} & \frac{y_r-y_2}{\rho_r^s} & \frac{z_r-z_2}{\rho_r^s} & 1 & 0 & 1 \\ \vdots & \vdots & \vdots & \vdots & \vdots & \vdots & \vdots & \vdots & \vdots \\ 0 & 0 & 0 & 0 & \frac{x_r-x_s}{\rho_r^s} & \frac{y_r-y_s}{\rho_r^s} & \frac{z_r-z_s}{\rho_r^s} & 1 & 0 & 1 \end{bmatrix} \tag{3.4.5}$$

And the residual matrix would be as follows:

$$
V = \begin{bmatrix} V_{P_{IF}^1} \\ V_{P_{IF}^2} \\ \vdots \\ V_{P_{IF}^s} \\ V_{f_{di}^1} \\ V_{f_{di}^2} \\ \vdots \\ V_{f_{di}^s} \end{bmatrix} \tag{3.4.6}
$$

Additionally, the unknown can be obtained by applying the following equation:

$$
\hat{x} = (A^T W A)^{-1} A^T W V \tag{3.4.7}
$$

For the code measurement noise, we assume the standard deviation denoted by $\sigma_{P_i}^s$. In the case of the *IF* combination, the corresponding variance should adhere to the law of error propagation. Therefore, the variance can be expressed as:

$$
(\sigma_{P_{IF}}^s)^2 = \left(\frac{f_1^2}{f_1^2 - f_2^2}\right)^2 (\sigma_{P_1}^s)^2 + \left(\frac{f_2^2}{f_1^2 - f_2^2}\right)^2 (\sigma_{P_2}^s)^2 \tag{3.4.8}
$$

For the Doppler measurement, the standard deviation is empirically determined as 0.03 m per second. Consequently, the weighting matrix W, incorporating this standard deviation, can be expressed as follows:

$$
W = \begin{bmatrix} \frac{1}{(\sigma_{P_{IF}}^s)^2} & & & & & & \\ & \frac{1}{(\sigma_{P_{IF}}^s)^2} & & & & & \\ & & \ddots & & & & \\ & & & \frac{1}{(\sigma_{P_{IF}}^s)^2} & & & \\ & & & & \frac{1}{(0.03)^2} & & \\ & & & & & \frac{1}{(0.03)^2} & \\ & & & & & & \ddots & \\ & & & & & & & \frac{1}{(0.03)^2} \end{bmatrix} \tag{3.4.9}
$$

Upon reaching the condition specified where the 3D position error becomes smaller than the pre-defined value of 0.01 m, the least-squares process concludes its iterations, and the final results are obtained as follows:

$$
\hat{X} = X^0 + \hat{x} \tag{3.4.10}
$$

3.5 Kalman Filter

The state vector comprises the position (x,y,z) and their corresponding velocities, the receiver clock offset, the system satellite clock difference, tropospheric zenith delay, as well as float carrier phase ambiguities. The system is first linearized, and then the discrete Kalman filter is applied. For the Kalman filter with a linear system at epoch k, it can be expressed as follows:

$$X_k = \phi_{k,k-1} X_{k-1} + v_{k-1} \tag{3.5.1}$$
$$L_k = H_k X_k + e_k \tag{3.5.2}$$

where,

- X_k stands for the state vector,

- L_k is the measurement vector,

- ϕ_k denotes the transition matrix,

- e_k and v_{k-1} refers to the measurement and the process noise vector, respectively, assumed as uncorrelated Gaussian white noise. The covariances of these noise vectors are denoted as R and Q.

The state vector is as follows:

$$x_k = \begin{bmatrix} x \\ y \\ z \\ cdt_r \\ \dot{x} \\ \dot{y} \\ \dot{z} \\ cd\dot{t}_r \\ Tro^s \\ T_{sys} \\ N_1 \\ N_2 \\ \vdots \\ N_s \end{bmatrix} \tag{3.5.3}$$

where N is the ambiguity information for each satellite. If there are s satellites in the study, the state vector would be $(10 + n) \times 1$. The NL combination is used as measurement, its corresponding variance matrix state R_n as:

$$R_n = \text{diag}\left((\sigma_{P_{IF}}^1)^2, (\sigma_{P_{IF}}^2)^2, \ldots, (\sigma_{P_{IF}}^s)^2, (\sigma_{L_{IF}}^1)^2, (\sigma_{L_{IF}}^2)^2, \ldots, (\sigma_{L_{IF}}^s)^2 \right) \tag{3.5.4}$$

The state vector and its covariance closely resemble the least squares approach. However, it is important to note that our method involves reference satellites. In the case of the reference satellite, we calculate its float values in terms of ambiguity. For all other satellites, the ambiguity, in practice, is defined as the difference between the ambiguity on L1 and that of the
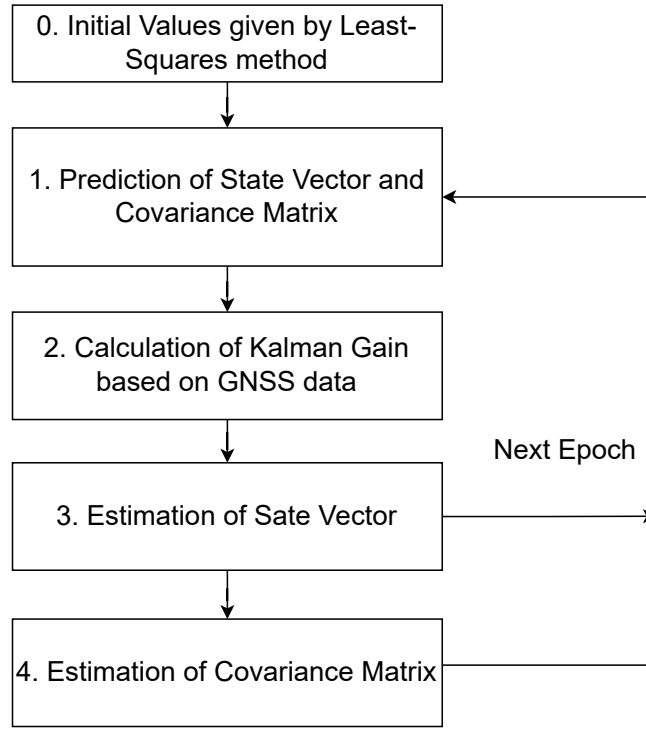
Figure 3.2: *General Steps of the Kalman Filter*

reference satellites. Each satellite system is associated with a specific reference satellite. The general procedures of the Kalman filter are summarized and illustrated in Figure 3.2.

In our method, once the initial values obtained from the LS method are combined with manually set parameters, e.g., initial values for ambiguities as 0, the Kalman filter predicts the next epoch state along with its covariance (Becker, 2018):

$$\hat{X}_{k,k-1} \quad = \quad \phi_{k,k-1} X_{k-1,k-1} \tag{3.5.5}$$
$$P_{k,k-1} \quad = \quad \phi_{k,k-1} P_{k-1,k-1} \phi_{k,k-1}^{T} + Q \tag{3.5.6}$$

and then using the so-called Kalman gain to decide how much we rely on the measurement:

$$K_k = P_{k,k-1} H^T (H P_{k,k-1} H^T + R_k)^{-1} \tag{3.5.7}$$

where R_k is the measurement noise covariance matrix. The final state vector and its uncertainty are computed based on the equations:

$$\hat{X}_{k,k} \quad = \quad \hat{X}_{k,k-1} + K_k(z_k - H\hat{X}_{k,k-1}) \tag{3.5.8}$$
$$P_{k,k} \quad = \quad (I - K_k H_k) P_{k,k-1} (I - K_k H_k)^T + K_k R_k K_k^T \tag{3.5.9}$$

When designing a navigation or positioning system, it is essential to consider how measurement noise and process noise weights impact the system's performance. Measurement noise and process noise weights will allow the system to trust which parts more. If the measurement noise is less than the process noise, the filter will rely more on the measurement than the system model. It is generally difficult to determine the process noise (Hauschild and Montenbruck, 2009).

3.6 PPP with Ambiguity Resolution

The exploration of unknown cycle ambiguities in phase measurement is crucial for achieving precise carrier phase measurements. This process involves resolving carrier-phase ambiguity to determine the integer property of float ambiguities. The general steps in ambiguity resolution methods typically begin with obtaining float ambiguities using algorithms like Least Squares or Kalman filter, representing the float solution. The subsequent step involves employing integer mappings or estimators, such as integer rounding (IR), integer bootstrapping (IB), and integer least-squares (ILS), to derive an integer solution. These values are considered fixed solutions only if the solution meets specific conditions, such as passing the ratio test. The GNSS model is then updated based on the contributions of these ambiguities.

3.6.1 Mixed-integer GNSS Model

The GNSS model for ambiguity resolution is derived from the observation equations 2.0.1 and 2.0.2. These equations are linearized to establish a system of linear equations, aiming to deduce the unknowns of interest, which include positions, tropospheric errors, and ambiguities. In the context of a mixed-integer model, it is assumed that the noise terms, ϵL_i and ϵP_i, in the observation equations are zero-mean random variables. This GNSS model can be expressed as follows:

$$y \sim \mathcal{N}(Aa + Bb, Q_{yy}), a \in \mathbb{Z}^n, b \in \mathbb{R}^p \qquad (3.6.1)$$

where,

- y vector contains the pseudorange and carrier-phase observables,

- $\sim$ denotes *distributed as*,

- $\mathcal{N}$ refers to the normal distribution,

- a describes an n-vector, the integer ambiguities,

- b represents a p-vector, the real-valued unknowns, such as position coordinates, atmospheric delay parameters, and clock parameters,

- (A, B) is the $m \times (n + p)$ matrix of full rank,

- Q_{yy} is the variance-covariance of the observations.

The objective of the ambiguity resolution step is to determine the integer constraints, $a \in \mathbb{Z}^n$, to achieve high precision for b. In most cases, the underlying probability distribution of the data is considered to be a multivariate normal distribution (Teunissen and Montenbruck, 2017).

3.6.2 Quality Control

There are three aspects discussed here. Firstly, the quality of the float ambiguity is assessed by the variance of the ILS or Kalman filter output. For example, if using the ILS method, $Q_{aa} = (A^T Q_{yy}^{-1} A)^{-1}$. Typically, the assumption is that the float ambiguity follows a multivariate normal distribution.

In the aforementioned methodology, such as IR, IB or ILS, integer values can typically be obtained for the float ambiguities. However, these methods are not flawless, and although they may yield integer values, these values may not accurately represent the true integer solution. Errors stemming from various sources or noise may obscure the integer characteristics, leading these methods to provide inaccurate estimates. Therefore, it is imperative to ensure the reliability of the integer ambiguities' output, specifically by assessing the success rate. To ascertain the success rate, it is crucial to understand the distribution of the integers, which is commonly assumed to follow a specific statistical distribution (Verhagen, 2004). Determining the success rate becomes pivotal in validating the accuracy of the integer solution. When the joint probability density function (PDF) of the float and fixed ambiguity is obtained, allowing the computation of the probability of $\check{a} = z$ by integrating over respective values like z. A key characteristic of the distribution of $\check{a}$ is evident: the likelihood peaks when a represents the correct integer as opposed to alternative estimated integers, as shown in the figure 3.3. Indeed, within the area of correct integer estimate, the integral of such a probability density function should reach its maximum. The success rate relies on this distinguishing feature. To ensure sufficient confidence in employing the fixed solution, it is advisable to set a threshold. Consequently, the fixed ambiguity would be accepted only when the success rate surpasses the predefined threshold. One should notice that the success rate is influenced by the choice of integer estimator and the precision of the float ambiguities (Teunissen and Montenbruck, 2017). It is a very important measure, since the fixed solution should only be used if there is enough confidence in this solution.
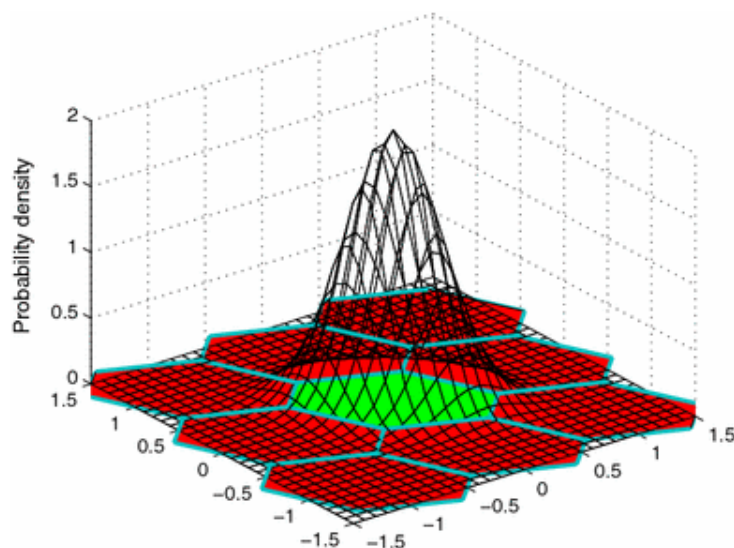

Figure 3.3: *Probability Density Function (PDF) in the ILS case, adapted from (Zhang et al., 2015)*

The integer solution quality is accessed by the ambiguity success rate, another crucial quality of interest is the fixed solutions which related to the position information. In the context of

our study, a fixed solution denotes that once the integer ambiguity is accepted, the position (x, y, z) computed by the Kalman filter or LS method is updated based on the residuals between the integer and float ambiguities. Therefore, if the success rate is significantly high (Teunissen and Montenbruck, 2017), the subsequent position vectors are updated based on the correlation between other parameter vectors (e.g., position coordinates) and the ambiguity vector. The updated fixed solution is expected to exhibit higher precision than that of the float solution.

The integer solution quality is accessed by the ambiguity success rate, while another crucial quality of interest is the fixed solutions related to position information. In our study, once the integer ambiguity is accepted, the position (x, y, z) computed by the Kalman filter or LS method is updated based on the residuals between the integer and float ambiguities (Teunissen and Montenbruck, 2017). The updated fixed solution is the so-called fixed solution. In other words, if the success rate is significantly high, the subsequent position vectors are adjusted based on the correlation between other parameter vectors (e.g., position coordinates) and the ambiguity vector. It is expected to exhibit higher precision than that of the float solution.

3.6.3 Integer Estimators

This subsection provides an in-depth explanation of integer mapping, focusing primarily on the IR, IB, and ILS methods. Here, we clarify how to use these methods and discuss the respective pull-in regions.

3.6.3.1 Integer Rounding (IR)

As the most straightforward integer resolution method, the rounding method involves rounding the float ambiguity to the nearest integer. The method is represented by the equation 3.6.2.

$$\check{a} = [\hat{a}] \tag{3.6.2}$$

where the symbol $[.]$ denotes for the rounding, and the estimated integer is expressed as $\check{a}$. Additionally, the definition of pull-in regions follows the equation below:

$$|\hat{a} - z| \leq \frac{1}{2} \tag{3.6.3}$$

This equation signifies that any float ambiguities $\hat{a} \sim \mathcal{N}(\hat{a} \in \mathbb{Z}, \sigma_{\hat{a}}^2)$ will be rounded to the integer z. The depiction of the pull-in region is further illustrated in the Figure 3.5. The red dot represents the float ambiguity, while the cyan dot represents the integer value. This implies that any red dot occurring within the square-shaped area is rounded to the central integer value, in this case, exemplified by 0.

3.6.3.2 Integer Bootstrapping (IB)

The concept of Integer Bootstrapping is associated with IR, and builds upon and extends the concepts introduced by IR. The procedure unfolds starts with assuming $\hat{\mathbf{a}} = (\hat{a}_1, \hat{a}_2, ..., \hat{a}_n)$. The method commences with $\hat{a}_1$, utilizing the integer IR method. The departure from both IB and
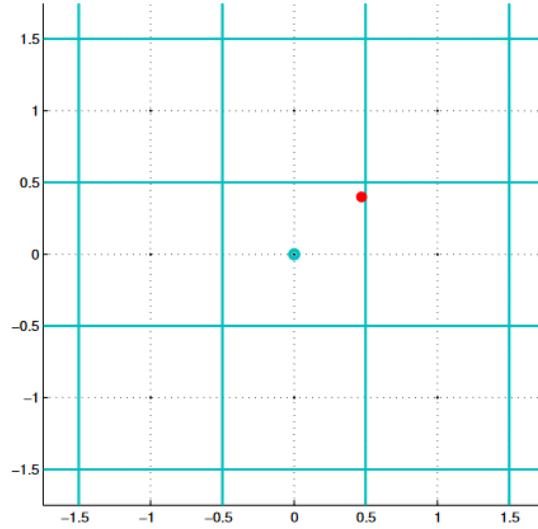
Figure 3.4: *The Pull-in Region of the Integer Rounding method (IR) (Verhagen et al., 2012)*

IR occurs here, where IB updates the remaining floating ambiguities based on the correlation between the rest and the first integer ambiguity. Subsequently, the newly updated float second ambiguity, repeats the same process as the first, obtaining integer values, updating the rest except the ones who already computed, and so on. To better comprehend these processes, the mathematical expressions are articulated as follows:

$$
\begin{aligned}
\breve{a}_{B,1} &= [\hat{a}_1] \\
\breve{a}_{B,2} &= [\hat{a}_{2|1}] = [\hat{a}_2 - \sigma_{21}\sigma_1^{-2}(\hat{a}_1 - \breve{a}_{B,1})] \\
&\vdots \\
\breve{a}_{B,n} &= [\hat{a}_{n|N}] = [\hat{a}_n - \sum_{j=1}^{n-1} \sigma_{n,j|J}\sigma_{j|J}^{-2}(\hat{a}_{j|J} - \breve{a}_{B,j})]
\end{aligned}
\tag{3.6.4}
$$

where $\breve{a}_{B,n}$ represents the nth ambiguity obtained through a conditioning on the previous sequentially rounded ambiguities (Necôulescu, 2022).

The above equation implies that the first float ambiguity $\hat{a}_1$ uses the rounding method. Subsequently, based on the correlation with the second float ambiguity ($\hat{a}_2$), the float ambiguity $\hat{a}_2$ is computed. The new float ambiguity then undergoes the IR method to obtain the integer. This process is repeated for the third float ambiguity, computed based on the correlation with the second one, and then fixed using the IR method. This sequence continues until the last float ambiguity $\hat{a}_n$ is resolved to a integer value $\breve{a}_{B,n}$.

Based on its information, the pull-in region can be depicted as Figure 3.5. Similar to the IR, any float within this parallelogram would be rounded to the central values. For instance, any red dot in this case within the certain area, corresponds to 1.
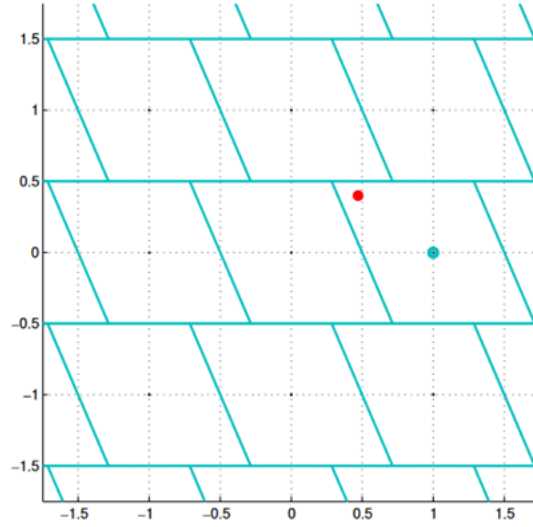
Figure 3.5: *The Pull-in Region of the Integer Bootstrapping method (IB) (Verhagen et al., 2012)*

3.6.3.3 Integer Least-Squares (ILS)

The absence of invariance against integer reparameterizations in IB and IR motivates researchers to investigate alternative methods, exemplified by the ILS method, as proposed by Teunissen (1993). Z-transformations play a crucial role in preserving the inherent nature of integer vectors even after transformation. This implies that: $|Q_{\hat{z}\hat{z}}| = |ZQ_{\hat{a}\hat{a}}Z^T| = |Q_{\hat{a}\hat{a}}|$. However, caution is warranted, as the lack of invariance in IB and IR does not inherently imply poor performance. Instead, the effectiveness of these methods depends on their success rate in a given situation, highlighting the importance of specific criteria for assessing their performance.

In the ILS method, unlike the straightforward computation in methods like IB or IR, a search step is necessary. After decorrelation, this search step, which provides the integer candidates for the float ambiguities, is constrained by the function:

$$||\hat{z} - z||^2 Q_{\hat{z}\hat{z}} \tag{3.6.5}$$

By employing the above equation, the obtained integer results should ensure that the distance between their integer vector and the float ambiguity vector is minimized. Consequently, the pull-in region for the integer z is determined as:

$$\mathcal{S}_{z,LS} = \{x \in \mathbb{R}^n \mid \|x - z\|_{Q_{\hat{a}}}^2 \leq \|x - u\|_{Q_{\hat{a}}}^2, \forall u \in \mathbb{Z}^n\} \tag{3.6.6}$$

After deduction and reorganization of Equation 3.6.6, the final form can be expressed as follows:

$$(u - z)^T Q_{\hat{a}}^{-1}(x - z) \leq \frac{1}{2}\|u - z\|_{Q_{\hat{a}}}^2 \tag{3.6.7}$$

Thus, it is demonstrated that the ILS pull-in region is constructed as an intersecting half-space, bounded by planes orthogonal to $(u - z)$ (Verhagen, 2004). Additionally, in the two-dimensional case, the pull-in regions are depicted as hexagons, as shown in Figure 3.6. It is

noticeable that the pull-in region takes the shape of a hexagon. The example yields an integer estimate of 1 for any red dot located inside this hexagon.
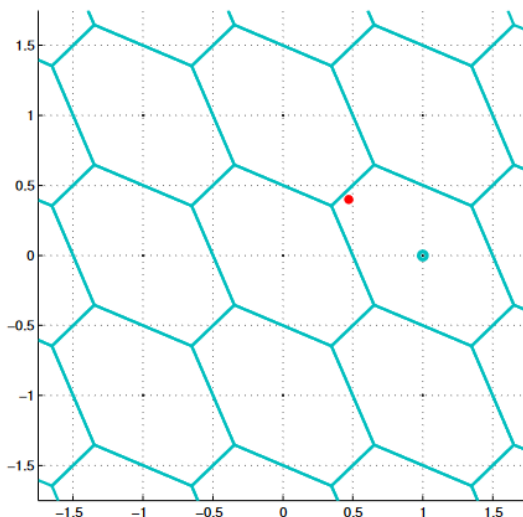

Figure 3.6: *The Pull-in Region of the Integer Least-Squares (ILS) Verhagen et al. (2012)*

3.6.3.4   Cases of the Integer Least-Squares

The LAMBDA, tackles an integer least-squares problem and comprises two steps. The initial step involves decorrelating the original float ambiguities to attain a more spherical shape, a process commonly referred to as Z-transformation. The following functions are employed in this step:

$$z = Z^T \hat{a}, \quad Q_{\hat{z}} = Z^T Q_{\hat{a}} Z, \quad \check{a} = Z^{-T} \check{z} \tag{3.6.8}$$

Internally, careful consideration should be given to the selection of Z to preserve the inherent integer nature of the ambiguities while also maintaining volume within the search space. This requirement is driven by the determinant of Z being equal to minus or positive 1 (Verhagen, 2004). The Figure 3.7 provides an illustration of how the Z-transformation impacts the search space. Indeed, it is evident that after the Z-transformation, the search space transitions from its original elongated shape to a more spherical form.

The second step involves exploring an optimal estimate or a set of optimal estimates for the parameter vector within a hyper-ellipsoidal region, resulting in the determination of integer ambiguity. The subsequent step is to employ a ratio test to decide whether the candidates are retained or discarded.

The mLAMBDA method is a modified version of LAMBDA, aiming to improve computational efficiency in both the transformation and search stages (Chang et al., 2005). This implies that it is related to decorrelate and search for optimal integer candidates efficiently in the float ambiguity solution obtained from the Kalman filter, provided that the WL Ambiguities are fixed. Furthermore, a residual test is implemented as a condition that prevents the candidates from
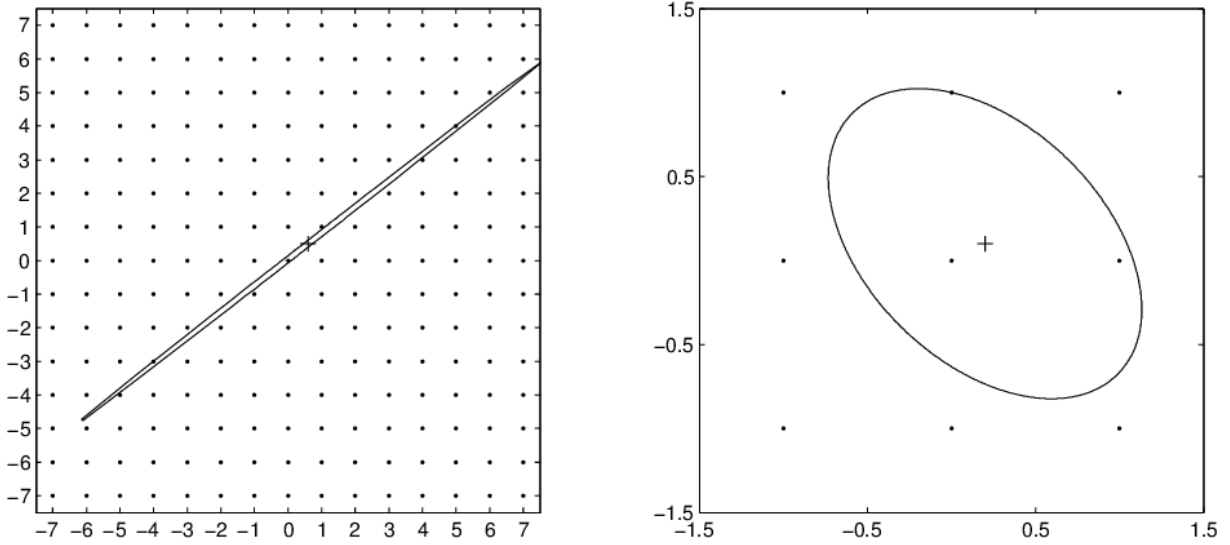
Figure 3.7: Comparison of the Search Space Before (left) and After (right) Z-transformation, adapted from Verhagen (2004).

being fixed when the differences between the predicted ambiguity and the final float ambiguity are significant and when the updated ambiguity value and the final float ambiguity are above the empirical values. Additionally, an empirical threshold of 3 for the ratio test was adopted in the PPP AR engine. Both tests were performed to give a high probability of correctness to the integer output of mLAMBDA. The "Fix and hold" strategy is a prominent feature of the approach. Once ambiguities are fixed, their corresponding Kalman filter initial values are set as integer values from the mLAMBDA with minimal variance, which indicates a high degree of confidence in the guess (Liu et al., 2023a).

Furthermore, the positions in the x, y and z directions will be updated based on the following equations:

$$\check{b} = \hat{b} - Q_{\hat{b}\hat{a}}Q_{\hat{a}\hat{a}}^{-1}(\hat{a} - \check{a}) \qquad (3.6.9)$$

$$Q_{\check{b}\check{b}} = Q_{\hat{b}\hat{b}} - Q_{\hat{b}\hat{a}}Q_{\hat{a}\hat{a}}^{-1}Q_{\hat{a}\hat{b}} \qquad (3.6.10)$$

where symbols with ˇ stand for the integer ambiguities, while those with ˆ refer to the float solutions. **b** represents the position's x, y and z components in ECEF coordinates, and the matrix **Q** denotes the covariance Teunissen and Montenbruck (2017). The matrix **a** represents the ambiguity group. These are differentiated by the suffix.

Chapter 4

Simulation Setup and Sensitivity Analysis Approach

This chapter offers a thorough overview of the simulation setup, encompassing details about the datasets employed in the experiments, the methods utilized for simulating input errors, and the criteria for determining convergence. Additionally, it delineates the PPP algorithm used throughout the entire set of experiments, specifically the PPP AR Engine. Finally, this chapter provides a thorough summary of all relevant experiments, including sensitivity analysis and model comparison, necessary for performance evaluation.

4.1 Simulation Setup

The dataset utilized in this study underwent simulation using Spirent's error-free mode to ensure that errors exclusively originated from introduced error types, such as satellite orbit errors, satellite clock errors, and troposphere errors. The overview of the satellites used in the thesis can be seen from the Figure 4.1. Numbers 1 to 50 correspond to GPS satellites, 51 to 100 represent GLONASS satellites, 101 to 150 indicate Galileo satellites, and 151 to 200 represent Beidou satellites. We confined our experiments to the GPS and Galileo systems, and the satellites' trajectories are illustrated in the plot. The majority of satellites were clearly visible, affirming their acceptance, as we empirically set the mask threshold to 5 degrees for the simulated data.

To minimize the impact of errors of interest, both the satellite and receiver-dependent phase, as well as code biases, which are typically calibrated, were set to zero. The Minimum Operational Performance Specification (MOPS) model usually introduces small multipath and tracking noise (SC-159, 2006). The mapping function of the troposphere delay is defined by Equation 4.1.6. Therefore, inspired by the MOPS model, the experiment was conducted in a static mode, simulating an open-sky condition. The convergence time is defined as the onset when the error is below 10 cm and remains so during at least 10 min. Additionally, all the standard deviations discussed were assumed in the line of sight.

As detailed in the previous chapter, the analysis of results focused on KPIs including position accuracy, convergence time, and fixing rate, which were evaluated within each experiment. For a comprehensive understanding of the processing strategy employed, please refer to Table 4.1:

In total, seven scenarios were executed in each experimental trial. Based on the PPP AR Engine, the first scenario was computed when all error sources were near to their intermediate values, denoted as "Base." From the second scenario onward, the standard deviation values (choosing
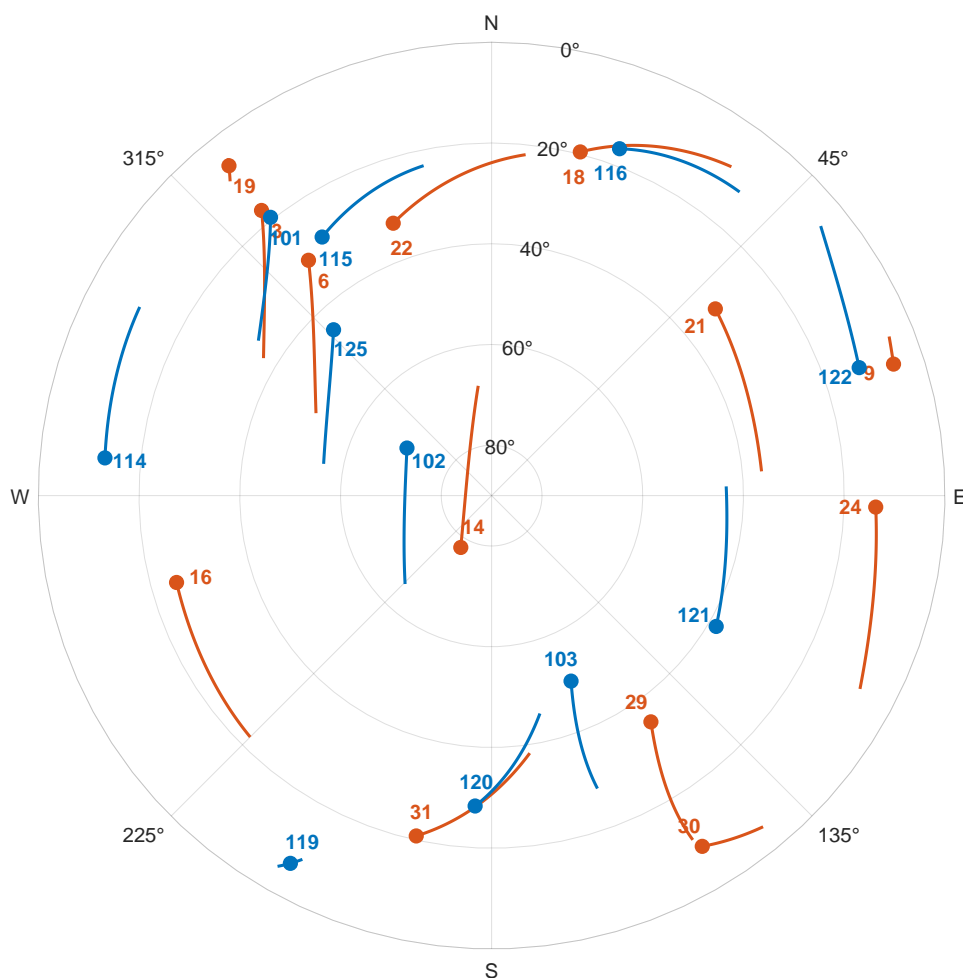
Figure 4.1: *Skyplot of Satellites during the Initial 3600 Epochs: GPS Satellites 1-50 in Red and Galileo Satellites 100-150 in Blue*

minimum and maximum values) for each error type (satellite orbit residuals, satellite clock errors, troposphere errors) were varied while keeping the rest of the error sources at their "Base" values.

Standard deviations (STDs) ranges for error types, with maximum possible reference to IGS product analysis reports (IGS, 2022), details can be found in the Table 4.2. The abbreviations "min" and "max" stand for minimum and maximum, respectively. It is important to note that the maximum STDs corresponds to the Ultra-Rapid IGS product, while the minimum value represents the best accuracy final product based on the IGS product report. "Orb," "Clk," and "Tro" represented satellite orbit error, satellite clock error, and troposphere error, respectively. In subsequent scenarios, when referring to a specific error type change, the corresponding abbreviation was used, specifying whether the minimum or maximum values were changed. As mentioned earlier, the other types of errors remained at the "Base" setting. It can be easily seen

***Table 4.1:** Description of Processed Items and Approaches.*

Processed Items	Approach
Processing mode	Static
Weighting scheme	Elevation dependent
Modelling of the measurements	Single differencing, WL + NL/IF combinations
Elevation mask	5°
Standard deviation of measurement noise	Phase: $0.004, 0.008, 0.02m$; Code: $0.2 - 0.5m$
Troposphere error	Estimated
Mapping function	nGPT2 + GMF
Relativistic effects	Yes
Adjustment method	Weighted Least-Squares, Extended Kalman Filter
mLAMBDA	Integer Least-Squares with Ratio Test and Residual Test
Process uncertainty of receiver position	0
Process uncertainty of receiver clock error	$3 \times 10^8 m$
Process uncertainty of the troposphere delay	$10^{-8} m$
Process uncertainty of the inter-system time difference	$10^{-6} m$
Process uncertainty of carrier phase ambiguities	$10^{-16} m$

that the error type with the largest variation is the satellite clock error, followed by the errors from the satellite orbit and the troposphere.

***Table 4.2:** Standard Deviations (STDs) Range for Error Types*

Error Source	Standard Deviation [m]		
	Minimum	Base	Maximum
Satellite Orbit	0.025	0.05	0.1
Satellite Clock	0.006	0.15	0.45
Vertical Troposphere	0.004	0.02	0.12

Additionally, the variations in variance for each error type in each scenario are depicted in Figure 4.2. One can gain an understanding of how the STDs change for each component in each scenario. This information complements Table 4.2.

For the errors arising from multipath and tracking noise (MN), the Airborne Accuracy designator A and B (AAD-A) from the MOPS model (SC-159, 2006) addressed them as follows:

$$\sigma_n(e) = 0.15 + 0.43 \exp\left(-\frac{e}{6.9}\right)$$
$$\sigma_{\text{mp}}(e) = 0.13 + 0.53 \exp\left(-\frac{e}{10}\right) \tag{4.1.1}$$
$$\sigma_{\text{mn}}^2(e) = \sigma_n^2(e) + \sigma_{\text{mp}}^2(e)$$
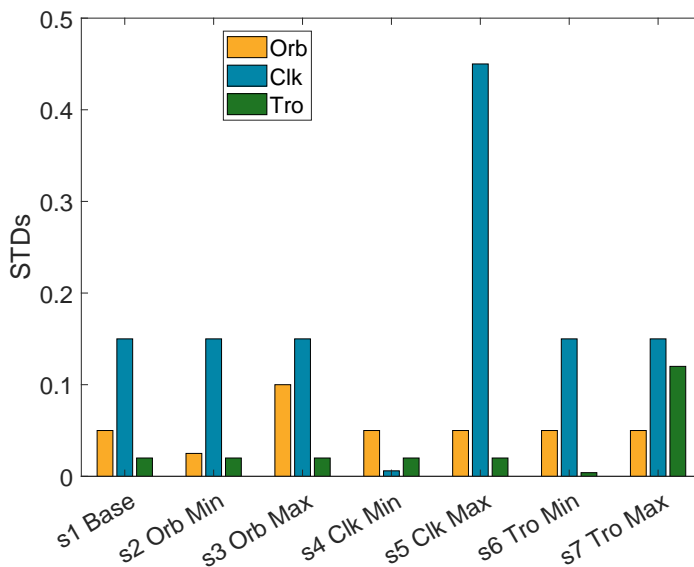
Figure 4.2: *Distribution of Individual Standard Deviation per Scenario*

The condition indicated when the system was influenced by multipath but with a relatively low impact. The multipath and noise impact corresponding STDs were computed based on Equation 4.1.1 for the satellites involved in the experiments. Figure 4.3 further displayed the standard deviations of the multipath and receiver noise details for each satellite involved in the measurements for the whole trials. The caption "SV" denotes the satellite vehicle, signifying satellites in the thesis. Thus, it is evident from the figure that only GPS and Galileo satellites are utilized in this context. It is worth noting that the maximum STDs from the multipath and tracking noise in the figure consistently remained below 0.5 m, while the minimum error hovered around 0.2 m. It is widely acknowledged that multipath and tracking noise exert distinct effects on the code measurements of *L*1 and *L*2 frequencies. Consequently, we generated two error sets by assuming a commonality in their standard deviations and random generator. This can be expressed as follows:

$$MN1(e) \quad \sim \quad \mathcal{N}(0, \sigma_{mn}^2(e)) \tag{4.1.2}$$

$$MN2(e) \quad \sim \quad \mathcal{N}(0, \sigma_{mn}^2(e)) \tag{4.1.3}$$

The following section describes two error input models aimed at elucidating the characterization of satellite orbit, satellite clock, and troposphere residuals or errors after applying their corresponding correction products. We have named these two models, White Gaussian Model (Method 1) and Autoregressive Model (Method 2) for distinction and ease of reference. The following provides a detailed explanation of each model, their formulations, and their application to express the behavior of the residuals in our correction methods. Finally, excluding previously mentioned error sources like orbital errors, troposphere errors, satellite clock errors, multipath and noises, no additional errors, such as antenna phase-related errors or biases, were introduced in the experiment.
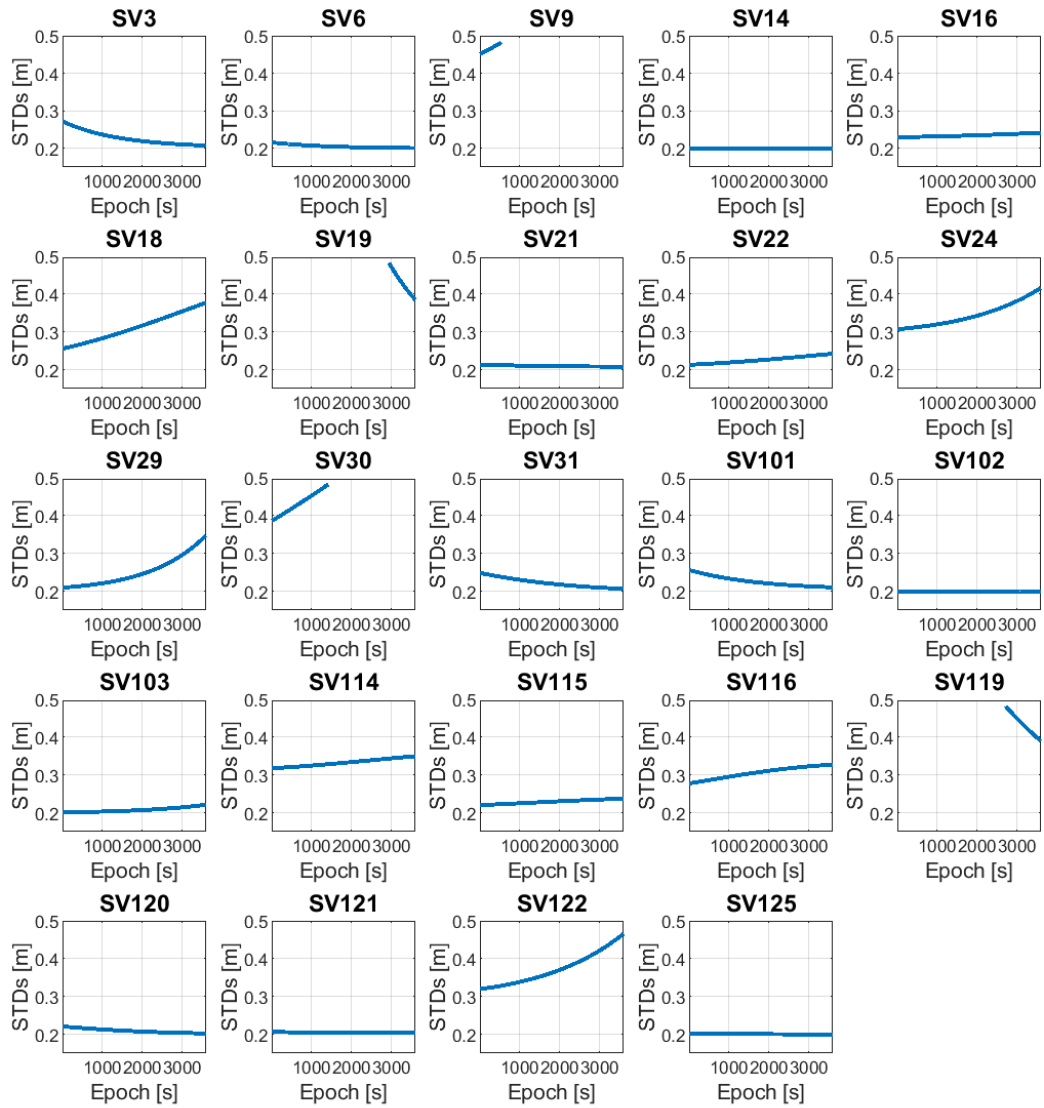
Figure 4.3: *Multipath and Tracking Noise Standard Deviations Dynamics in Satellite Observations*

4.1.1 White Gaussian Model - Method 1

In this model, the residual errors of interest were described by using a White Gaussian Noise process. At this stage, our focus is solely on the impact of residuals on the pseudorange, with the phase measurement constrained within a 4 mm range of noise. As for the satellite orbit and satellite clock residuals, they were generated by:

$$^G\text{Orb} \sim \mathcal{N}(0, \sigma_{\text{Orb}}^2) \tag{4.1.4}$$

$$^G\text{Clk} \sim \mathcal{N}(0, \sigma_{\text{Clk}}^2) \tag{4.1.5}$$

where,

- the upper sign G indicates White Gaussian method.
- *Orb* means the orbital error for the i-th satellite.
- σ_{Orb}^2 is the variance for the orbital error.
- *Clk* refers to the satellite clock error for the satellite.
- σ_{Clk}^2 stands for the variance (standard deviation squared) for the clock error.

In terms of the tropospheric error, it was simulated based on the following equations 4.1.8:

$$m(e) = \frac{1.001}{\sqrt{0.002001 + \sin^2(e)}} \tag{4.1.6}$$

$$\sigma_{trop}(e) = \sigma_{TVE} \cdot m(e) \tag{4.1.7}$$

$$^G\text{Trop}(e) \sim \mathcal{N}(0, \sigma_{trop}^2(e)) \tag{4.1.8}$$

where,

- σ_{TVE} stands for the tropospheric vertical error.
- σ_{trop}^2 is the troposphere error variance.
- $m(e)$ means the mapping function.
- *Trop(e)* is used for as the tropospheric error.

The residuals from the preceding equations, representing satellite clock, orbit, and troposphere errors, were combined as follows:

$$^G\text{OCT}_{res} = {}^G\text{Orb} + {}^G\text{Clk} + {}^G\text{Trop}(e) \tag{4.1.9}$$

Ultimately, all the previously mentioned errors, in addition to the effects of multipath and tracking noise from Equations (4.1.2) and (4.1.3), were collectively integrated into the code measurement domain:

$$^G\text{PR1}_{\text{res}} = {}^G\text{OCT}_{\text{res}} + \text{MN1}(e) \tag{4.1.10}$$

$$^G\text{PR2}_{\text{res}} = {}^G\text{OCT}_{\text{res}} + \text{MN2}(e) \tag{4.1.11}$$

As for the phase measurement, the standard deviation of the noise was 4 mm, and the phase noises (CP1, CP2) were generated by Gaussian random noise:

$$^{G}\text{CP1}_{\text{res}} \quad \sim \quad \mathcal{N}(0, 0.004^2) \tag{4.1.12}$$

$$^{G}\text{CP2}_{\text{res}} \quad \sim \quad \mathcal{N}(0, 0.004^2) \tag{4.1.13}$$

4.1.2 Autoregressive Model - Method 2

The adoption of an autoregressive (AR) model served the purpose of generating more realistic error processes, including autocorrelation of the noise. This choice was inspired by the utilization of Gauss-Markov processes in code measurement, as discussed by Rankin (1994). We implemented the AR model with a constant value, and the first order was represented as follows (Wikipedia contributors, 2023):

$$x_t = \phi x_{t-1} + \varepsilon_t \tag{4.1.14}$$

The parameter ϕ significantly influences the stability of the series; the closer it is to 1, the more normally distributed the series becomes according to the central limit theorem. In another word, if ϕ is small, the autocorrelation decays rapidly, approaching a white Gaussian noise. Conversely, when ϕ is close to 1, the autocorrelation function decays slowly, indicating strong autocorrelation in the data. On the other hand, the noise intensity ε_t determined the degree of fluctuation in the series. The corresponding variances can be approximated as:

$$\sigma_{x_t}^2 = \frac{\sigma_{\varepsilon_t}^2}{1 - \phi^2} \tag{4.1.15}$$

σ_{x_t} in Equation 4.1.15 represented the standard deviation of x_t, and it was derived from our initial settings Table 4.2. These settings included the minimum, maximum, and nominal conditions established in the preceding steps.

We systematically vary the parameter ϕ to tailor the auto-correlation of errors. This adjustment was crucial for ensuring the desired temporal characteristics. Specifically, a designated period τ was introduced to regulate the duration of changes within the fixed sampling rate Δt, set at 1 second:

$$\begin{aligned} \alpha &= \frac{\Delta t}{\tau} \\ \phi &= 1 - \alpha \end{aligned} \tag{4.1.16}$$

We explored various settings for the time constants τ associated with different error sources. In our assumptions, 10 min, 30 min, and 1 day corresponded to satellite orbit, satellite clock, and troposphere errors, respectively, as illustrated in Figure 4.4. For future endeavors, selecting parameters should be based on long-term measurement data, e.g., from IGS. The values we assigned resulted in ϕ being very close to 1 for each error type, indicating a strong positive autocorrelation. In other words, the values in the time series were highly correlated with their
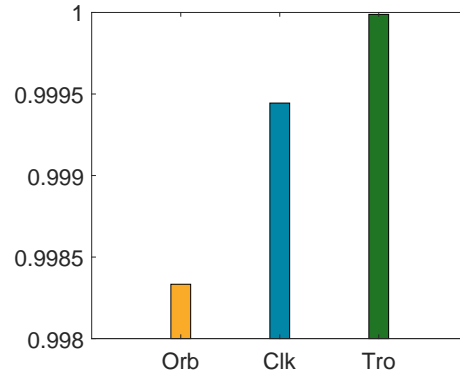
Figure 4.4: φ Value for Each Error Type

preceding values. We initially surmised that the troposphere errors exhibited the most autocorrelated behavior among the error types. For a more realistic τ, further investigation is required.

Based on Equation (4.1.15), we can compute different σ_ϵ for the Gaussian noise in our AR(1) model. The Gaussian noise of the AR system was generated based on a normal distribution with a mean of 0 and standard deviation σ_ϵ:

$$\varepsilon_{\text{tp}} \sim \mathcal{N}(0, \sigma_{\text{tp}}^2) \tag{4.1.17}$$

where, tp stands for the error type, which can be residuals from satellite orbit(Orb), satellite clock (Clk), and the troposphere error (Tropo). The details can be found from the Figure 4.5.
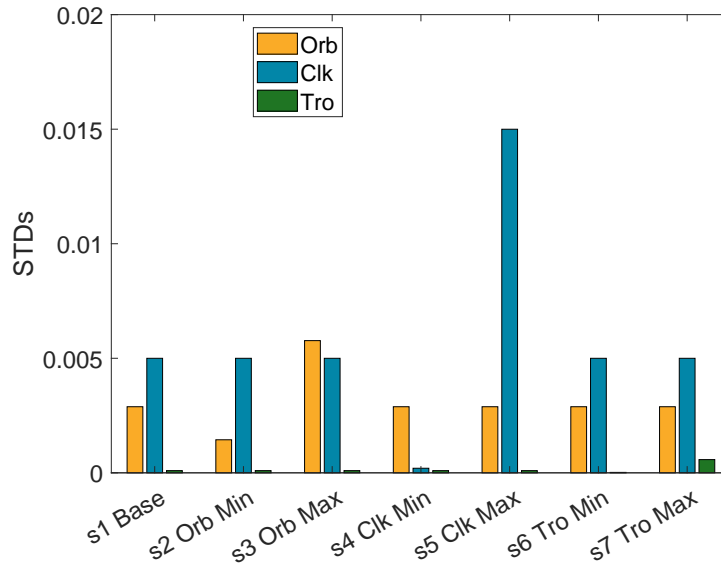
Figure 4.5: Distribution of Gaussian Noise Standard Deviation per Scenario

Furthermore, the initial values were generated from Gaussian random noise based on their corresponding STDs and with 0 mean value. From the first epochs, the simulations of errors

would follow the AR model. The multipath and tracking noise for the code measurement were still determined by equations 4.1.2 and 4.1.3.

In total, the errors generated by Method 2 on the top of code measurements were expressed as:

$$^A\text{OCT2}_\text{res} = {}^A x_{t,\text{Orb}} + {}^A x_{t,\text{Clk}} + {}^A x_{t,\text{Tropo}} \tag{4.1.18}$$

Where the upper sign "A" stands for the AR model. As for the phase measurement noise, we randomly generated it with a normal distribution of zero mean and given standard deviations (σ_{cp}) into $L1$ and $L2$ frequencies. Therefore, the final errors and noises in the code and phase measurements were as follows:

$$
\begin{aligned}
^A\text{PR1}_{res} &= {}^A\text{OCT2}_\text{res} + \text{MN1}(e) & (4.1.19) \\
^A\text{PR2}_{res} &= {}^A\text{OCT2}_\text{res} + \text{MN2}(e) & (4.1.20) \\
^A\text{CP1}_{res} &\sim \mathcal{N}(0, \sigma_{cp}^2) & (4.1.21) \\
^A\text{CP2}_{res} &\sim \mathcal{N}(0, \sigma_{cp}^2) & (4.1.22)
\end{aligned}
$$

4.2 PPP AR Engine Processing Strategy

Although our experiments focused mainly on the filtering part, in this section we give a general overview of the processing of the engine. The PPP AR engine runs through simulated data and is implemented through the following processing steps: data handling, preprocessing, error modeling, filtering, and analysis.

4.2.1 Data Handling

This step involves the procedure of importing data from observation files in RINEX format and the precise products such as satellite clock and orbit correction information in SP3 format. Additionally, the relevant data will be decimated and organized into a matrix for subsequent processing.

4.2.2 Data Preprocessing

This phase of the PPP AR Engine serves the purpose of interpolating satellite orbit and velocity information, primarily chosen for its capability to accommodate smaller sampling rate. Furthermore, it involves masking out satellites with elevation below a certain threshold. In our simulated data, this threshold is set at 5 degrees to ensure a robust signal. Additionally, within this process, there are steps for detecting cycle slips, handling clock jumps, and detecting outliers. Specific methods for processing these issues are detailed in the accompanying Table 4.3.

Table 4.3: *Description of processed items and approaches.*

Processed Items	Approach
Satellite orbit and velocity interpolation	10th degree Lagrange interpolation
Elevation mask	Depending on thresholds
Cycle slip detection and repair	MW and Geometry-Free combination
Outlier detection and removal	Linear regression
Clock jump detection	Method proposed by Zhang et al. (2014)

4.2.3 Error modelling

Since the engine was primarily designed for simulated data, it is possible to manipulate the sources of error in a controlled manner. The error modeling is based on the errors introduced from the measurements. For example, if relativistic clock effects and tropospheric delays from satellites are introduced into the simulation, the errors they produce can be corrected by applying relativistic effect corrections and tropospheric model corrections. A general overview of the error modeling can be indicated in the table:

Table 4.4: *Description of Error modelling items and methods*

Error Items	Method
Dry troposphere	Saastamoinen model
Wet troposphere	nGPT2 + GMF
relativity	Kouba (2009)
Satellite clock offset	Precise emphemeris file,e.g. SP3

However, it should be noted that, due to our dataset being error-free, after the error modeling process, the mentioned items were set to 0. In our actual experiments, a new troposphere mapping function (see Equation 2.3.2) from the MOPS model was employed.

4.2.4 Filtering

This stage is a key component of the algorithm, allowing users to determine their position. As depicted in Figure 3.1, the process comprises distinct phases. In the initial stage, errors are intentionally introduced based on the input error models which we define. Subsequently, the SDWL combination is employed, and its ambiguity plays a pivotal role in determining the subsequent steps. If the ambiguity is successfully fixed, the subsequent step involves the new combination - NL combination. In the case where the ambiguity remains unresolved, the corresponding method entails using the Ionosphere-Free combination. These values serve as inputs or observations for the Kalman filter. The output will undergo further processing by mLAMBDA, resulting in either fixed or non-fixed ambiguities. Additionally, for the initial values of the Kalman filter, in instances where no satellites are fixed, they retain their previous values in terms of ambiguities, indicating a float solution. Conversely, if satellites are fixed, the initial values utilize the fixed values of the ambiguities.

4.3   Analysis strategy

In our experimental design, we executed a series of trials to evaluate the performance of various input error models and to explore how KPIs respond to different error variations. The experimental framework involved conducting multiple trials, most of which were repeated 100 times to ensure reliability. Notably, the second trial was an exception, with an extensive 1000 runs, highlighting its significance in our study.

The first two trials were particularly focused on "Method 1", which utilized a Gaussian-generated random noise model. The primary aim of these initial trials was to identify the optimal number of Monte Carlo iterations. This choice was critical for balancing the accuracy of results with the efficient use of computational resources and time

From the insights gained in these initial trials, we identified that 100 runs were sufficient for our PPP AR Engine analysis. Consequently, we employed this approach in the subsequent experiments. Shifting the focus to the remaining trials, our attention centered on the AR model. Here, we delved into the autocorrection of residuals and their impact on the KPIs. Additionally, we conducted experiments to scrutinize the phase noise effect on the behaviors of the AR model.

Chapter 5

Numerical Results

Numerical results, interpretation, and sensitivity analysis are presented in this chapter, with processing steps following the detailed description in the previous Chapter 4. The entire set of results is divided into three subsections focusing on convergence time, fixing rate, and position accuracy:

- A comparison of 100 and 1000 Monte Carlo simulation runs and the impact on result stability.

- An evaluation of different input error models, including different auto-correlation degrees within the AR model group.

- The impact of phase noise levels within the AR model while maintaining code noise and residuals constant.

In our study, we conduct a thorough analysis by looking at their CDF for key parameters, including convergence time, fixing rate, and position error. These CDFs were derived from a substantial number of simulation runs, specifically 100 as sufficient based on the first results subsection. This analysis provides a detailed understanding of parameter variations throughout the experiments, offering robust support for interpreting the experimental results.

5.1 Number of Simulation Runs Impact on Stability in Monte Carlo Results

The experiment employs Monte Carlo simulation to approximate the behavior of errors or uncertainties in the correction models through random sampling. It is widely acknowledged that a higher number of simulations leads to more stable results. However, due to computational constraints and time considerations, a logical approach is needed to conduct the experiments. In order to determine the optimal run times while maintaining the reliability of the results, we conducted 100 and 1000 runs using the Gaussian approach with the same setup.

As mentioned earlier, there are seven scenarios, with "Base" representing the condition where errors exhibit intermediate standard deviation values for satellite orbit, satellite clocks, and troposphere. In the subsequent scenarios, only the error type of interest varies, while the other parameters remain set at the "Base" conditions. The dashed lines indicate the minimum standard deviation for the corresponding error type, while the basic settings are maintained for the remaining types. Similarly, the solid line indicates the standard deviation for the maximum condition.

Figures 5.1, 5.2, and 5.3 summarize the empirical findings pertinent to our discussion. In detail, we computed the distributions across these runs for those KPIs, resulting in their respective CDFs.

The subplots in the first row of Figure 5.1 illustrates the influence of simulation times on the CDFs of convergence time for each scenario. The x-axis represents convergence time, while the y-axis depicts CDF values. Upon initial inspection of both subfigures, almost all solid lines are situated to the right of "Base," with dashed lines to the left. This consistent trend across both figures suggests that a runtime of 100 units is adequate for the used PPP AR Engine, providing sufficient data for statistical analysis.

Moving to the fixing rate aspect, the second row subplots from the Figure 5.1 display the CDF of the Wide Lane fixing rate. Notably, dashed lines are positioned to the right compared to the solid line, aligning with the observation that smaller residuals correspond to larger fixing rates. Moreover, all scenarios exhibit fixing rates exceeding 90%, indicating a high level of confidence in utilizing the mLAMBDA procedure to address narrow lane ambiguities. The parallel trends in both panels reinforce the conclusions drawn from the Convergence time comparison.

Examining the CDF of Narrow Lane fixing rate from the last row of Figure 5.1, both charts corroborate the findings from the CDFs of convergence time and Wide Lane fixing rate. The overall fixing rate converges around 30-40%, attributable to the restricted Narrow Lane fixing rate influenced by the stringent residual test. To deepen our understanding of the fixing rate, Figure 5.2 presents the averages, with Wide Lane fixing rates denoted by "star" symbols and Narrow Lane fixing rates by "dot" symbols. The x-axis conveys scenario information, while the y-axis indicates fixing rate values in percentage. Clearly, Wide Lane fixing rates approach 100%, whereas Narrow Lane fixing rates hover around 40%.

In terms of the position error, Figure 5.3 underscores that all position errors in both plots are nearly below 0.01 m, affirming that a runtime of 100 units suffices for our research objectives. Additionally, it substantiates that our convergence time is within the specified conditions, which is accurate.

However, all the previously discussed sets of data suggest that the S4 scenario is distinct compared to the other scenarios in terms of simulation run times. By looking into the convergence time for each experiment, there are more instances of convergence time exceeding 1000 s in the 1000 runs, while for the 100 runs, only a few show significant jumps, and their magnitudes are smaller than 500 s. This could be caused by outliers resulting from the randomness of the Monte Carlo simulation. It is not evident when the simulation times are low, but it becomes apparent as the times increase.

Additionally, both the narrow lane fixing rate and the position error exhibit a similar discrepancy in the 4th scenario. It is obvious that there are many more trials in the 1000 runs showing a lower fixing rate compared to the 100 runs. This may be the reason that S4 is showing inconsistency for the two conditions. For the Position error, similar explanations apply.

In summary, the pivotal conclusion is that the execution of 100 experimental runs yields a sufficient dataset for subsequent testing. While the utilization of extended run times could offer advantages, given researchers additional experimentation opportunities and access to advanced computational resources, the robustness of statistical outcomes derived from 100 runs renders them a pragmatic and feasible choice, particularly within the constraints of research timing resource limitation.
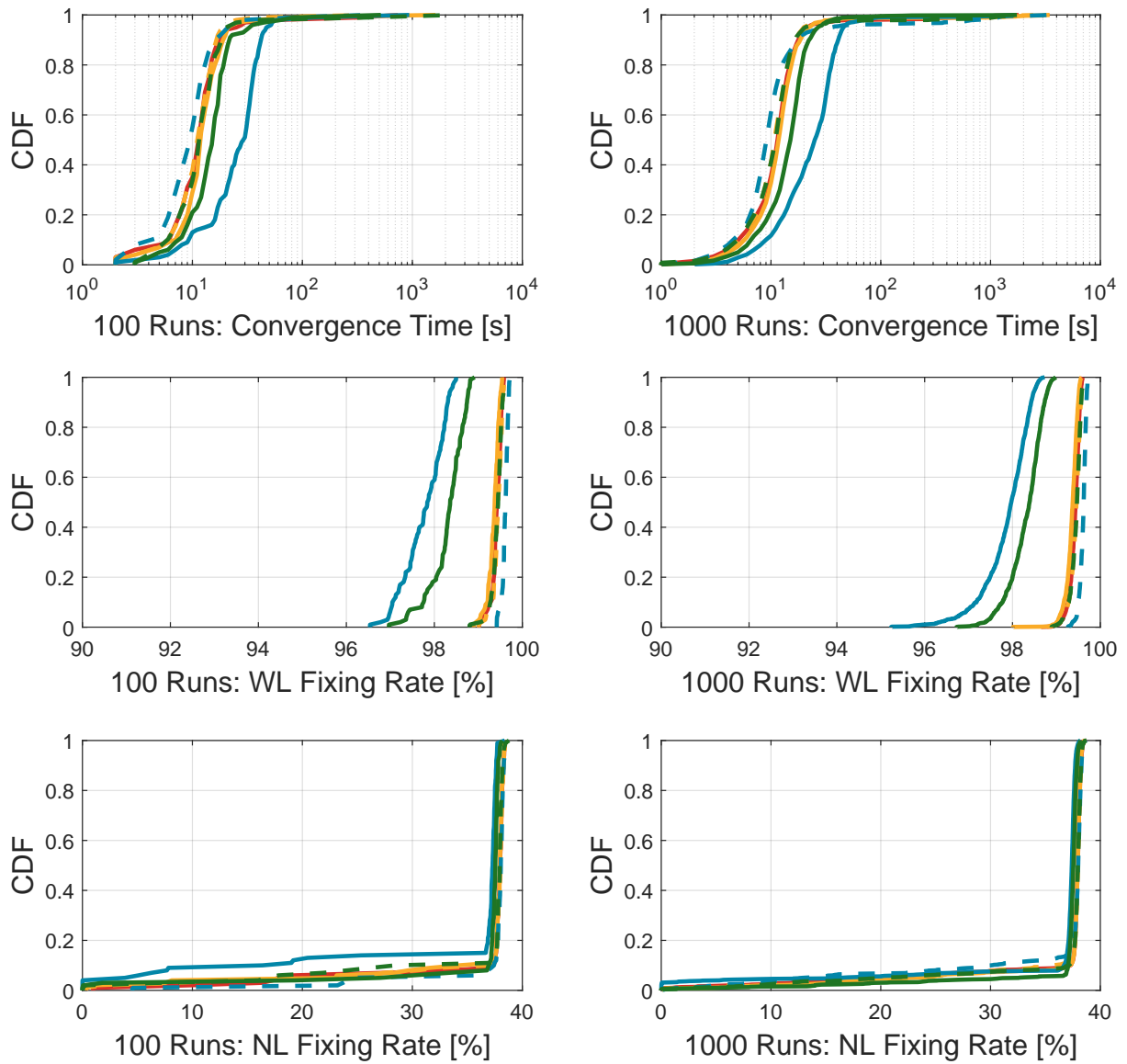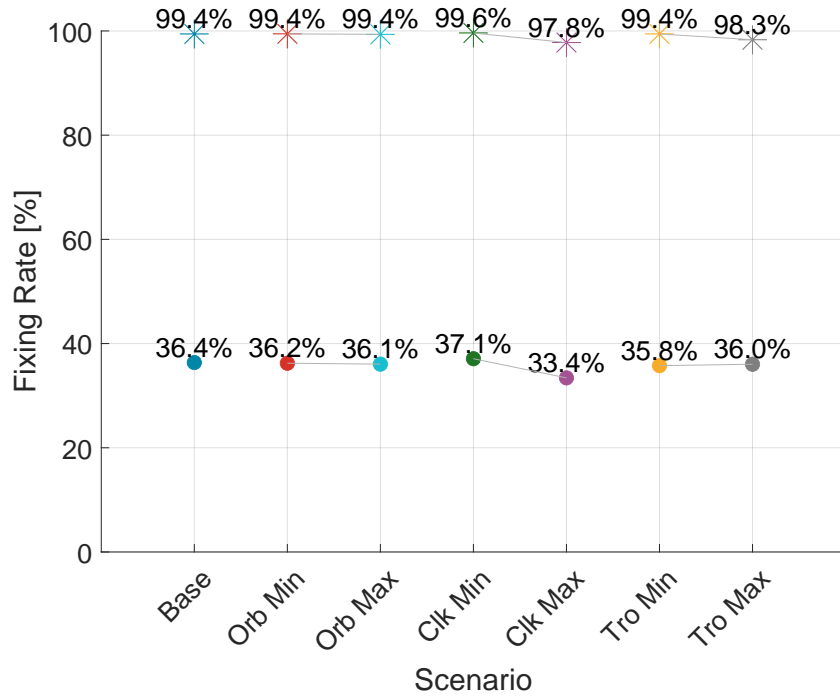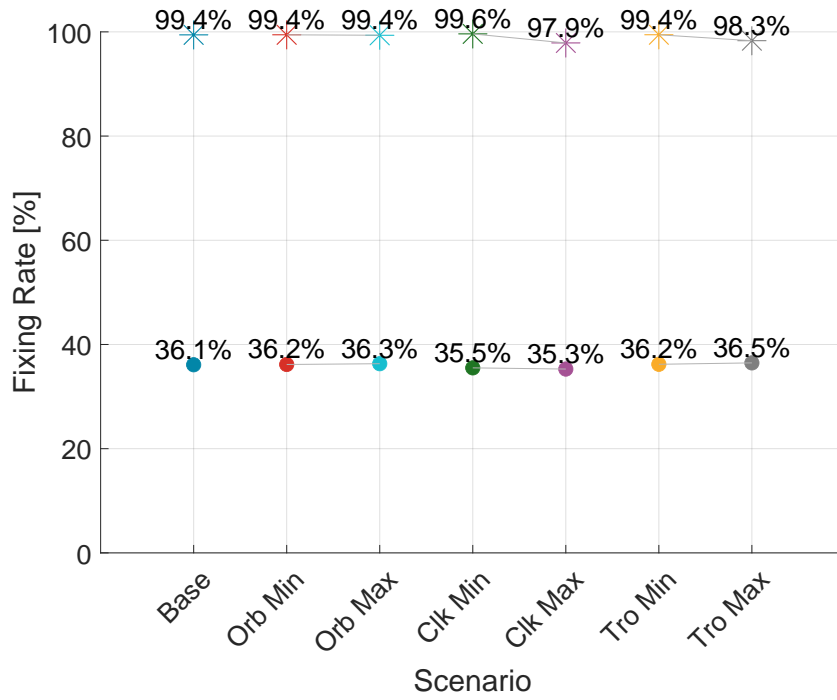
Figure 5.1: *Cumulative Distribution of Convergence Time and Fixing Rate Across Varying Monte Carlo Simu-*
lations: The solid red line represents the "Base" case, while dashed and solid orange lines correspond to the
scenarios "Orb Min" and "Orb Max". Blue lines indicate the scenarios "Clk Min" and "Clk Max", and green
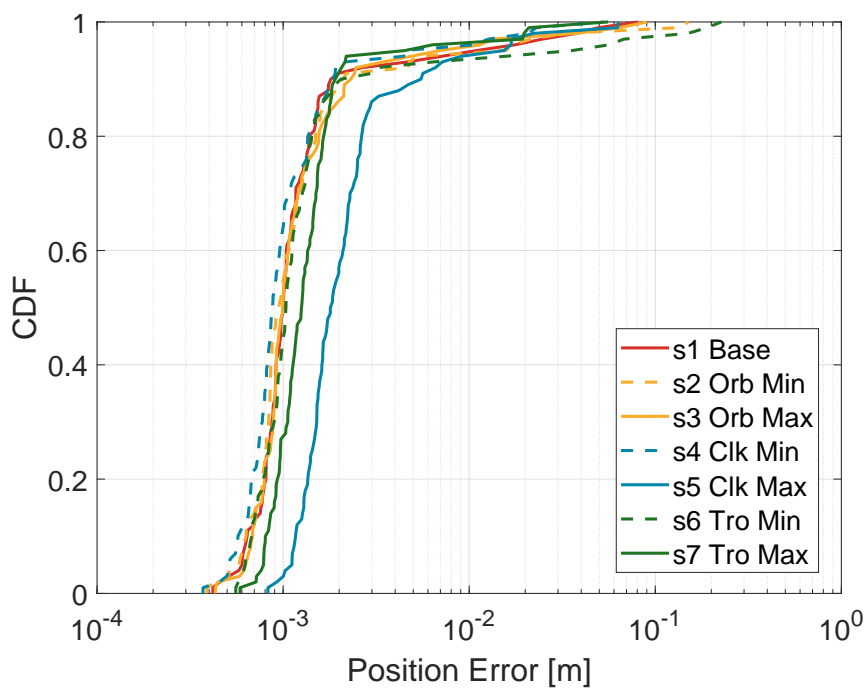*lines represent the scenarios "Trop Min" and "Trop Max".*
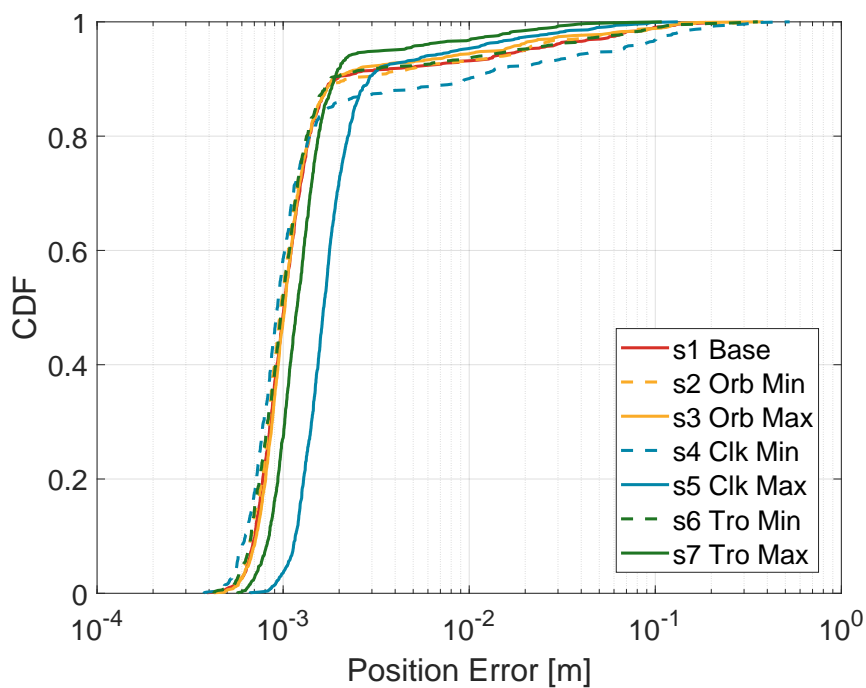
(a) 100 Runs

(b) 1000 Runs

Figure 5.2: *Mean Fixing Rate Across Varying Monte Carlo Simulations: ⋆ denotes WL, and · refers to NL*

(a) 100 Runs

(b) 1000 Runs

Figure 5.3: *Cumulative Distribution of Position Error Across Varying Monte Carlo Simulations*

5.2 Comparative Analysis of Models and Autocorrelation Examination

The following set of plots, Figure 5.4, 5.5, 5.6, 5.7, and 5.8, primarily illustrates the influence of various error models and the distinct effects of different autocorrelations on the outcomes. The comparison involves two input residual simulation models: the Gaussian model and the AR model. Specifically, the White Gaussian model represents a condition with no autocorrelation between the input values. In contrast, the AR model is characterized by increasing autocorrelation effects in the other two cases.

The results depicted in 5.4 illustrate the cumulative distribution function of convergence for different scenarios across various models. The three plots, labeled from a to c, depict conditions where the time constant for error types varies from small to large. For example, in the satellite orbit error group, the time constant is set to 1s, half of the original time (i.e., 300s), and the original time (i.e., 600s). These conditions correspond to autocorrelation levels ranging from low to high. In the three plots, all solid lines are on the right side when compared to the "Base" scenario, whereas dashed lines are closer to the left. This observation confirms the correctness of the model to some degree. In reality, larger residuals and poorer correction products typically lead to longer convergence times. Regardless of their specific values, the most substantial impact on convergence time occurs when varying the standard deviations of the satellite clock group. The second most significant change arises from altering the troposphere standard deviation, while the least pronounced effect is observed in relation to the orbit. This is a commonality shared by both models.

However, there is a key difference. The outcomes of the AR model exhibit a broader range in convergence time, whereas the Gaussian model tends to center around a more consistent value. This implies that the convergence times provided by the AR model, when only the input error models change, are larger compared to those of the Gaussian model. Additionally, the convergence times from the AR model exhibit a greater degree of dispersion. Furthermore, as the autocorrelation of the residuals increases, there is a tendency for a slightly longer convergence time.

In terms of the fixing rate, Figures 5.5, 5.6, and 5.7 illustrate the performance. The Wide Lane fixing rate, as depicted in Figure 5.5, undergoes significant variations when different error input models are employed. In the Gaussian group, almost all Wide Lane fixing rates are close to 100%, while the AR model predominantly shows rates in the range of 20-50%, with the exception of scenario 4, which exhibits a less pronounced drop. Similarly, the Narrow Lane fixing rate depicted in Figure 5.6 reflects a substantial decrease, dropping from the previous range of 35-40% across all scenarios to approximately 15-20%. Scenario 4, however, shows a less significant decrease in fixing rate. These phenomena are more clearly observable from the mean values of the fixing rate presented in Figure 5.7. Furthermore, with an increase in autocorrelation, the fixing rate both Wide Lane and Narrow Lane tends to decrease.

Regarding the position error, as denoted in Figure 5.8, the findings align with the above key performance indicators. The Gaussian model exhibits significantly less position error, while AR models tend to yield larger errors, with the majority being approximately one magnitude larger. Additionally, an increase in autocorrelation corresponds to a less precise position.
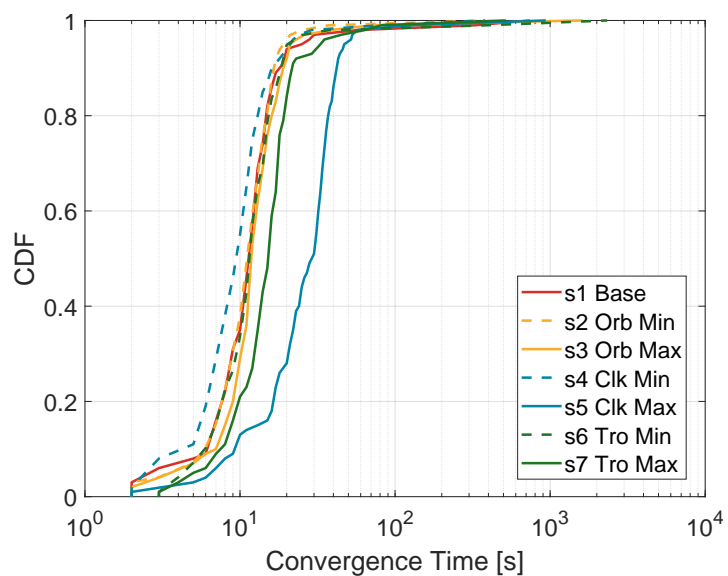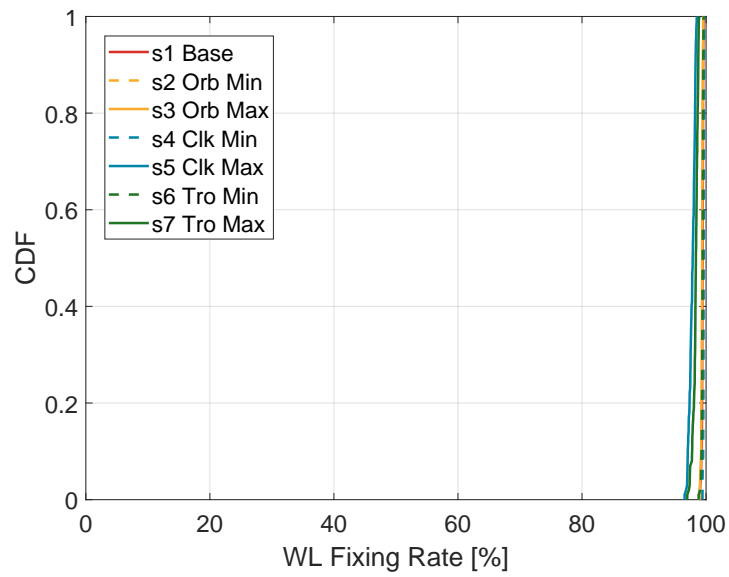
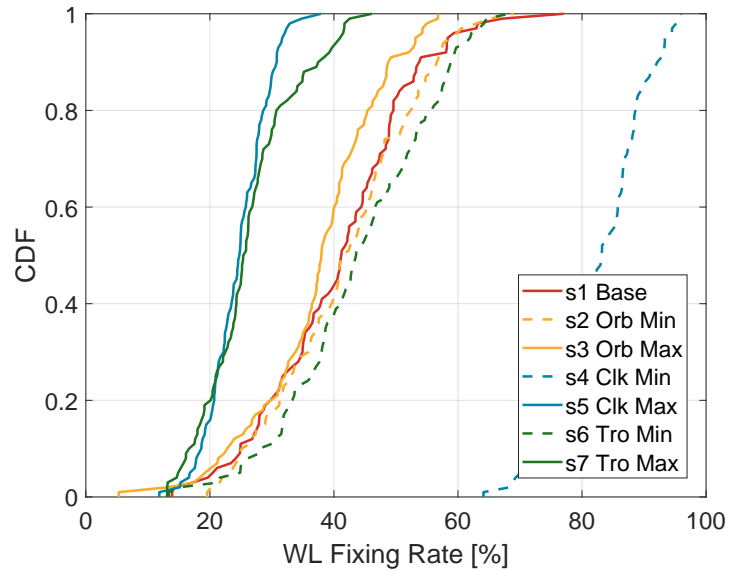(a) Gaussian Model
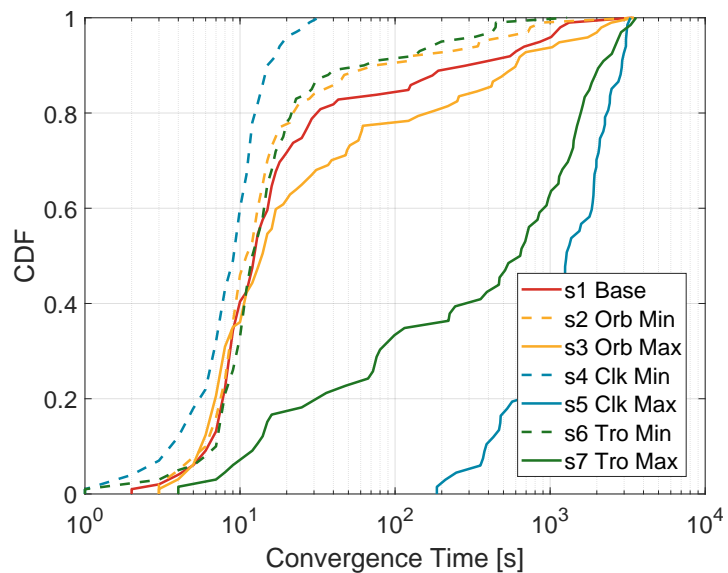
(b) AR Model (Low Autocorrelation)
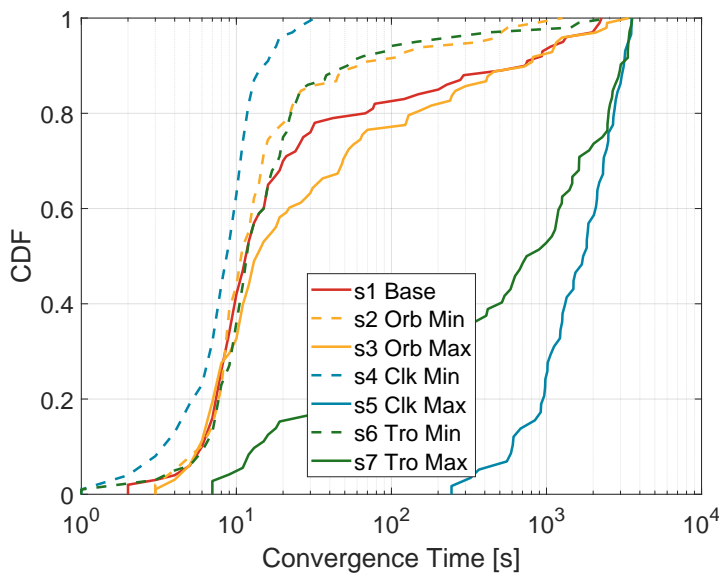
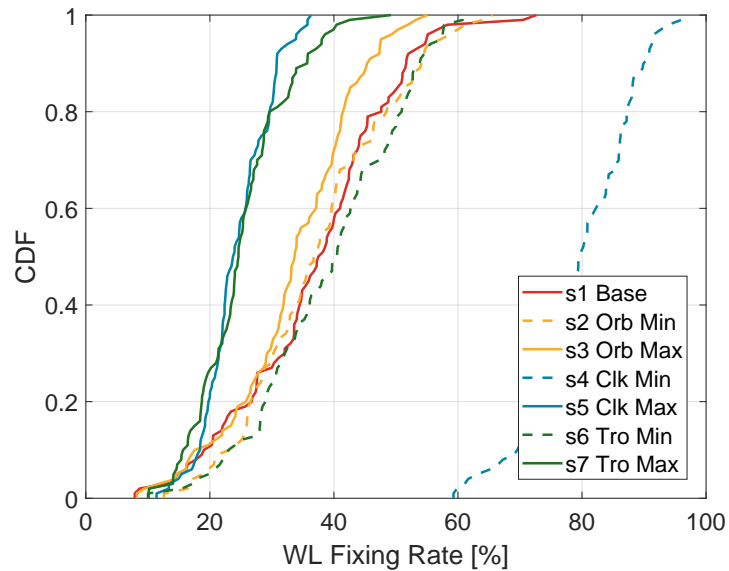(c) AR Model (High Autocorrelation)

Figure 5.4: *Cumulative Distribution of Convergence Time Across Different Residual Simulation Models*
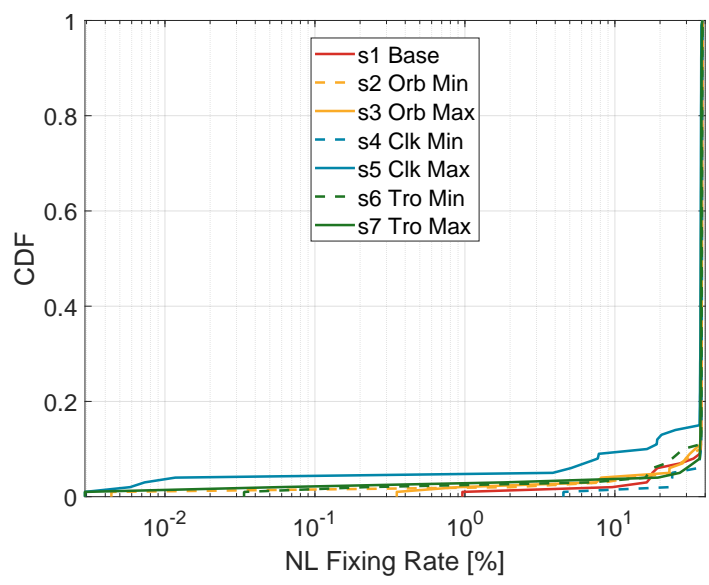
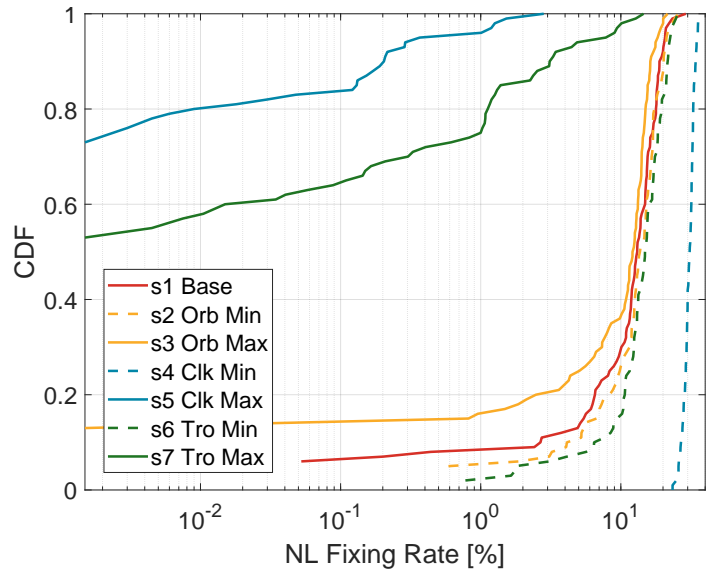(a) Gaussian Model

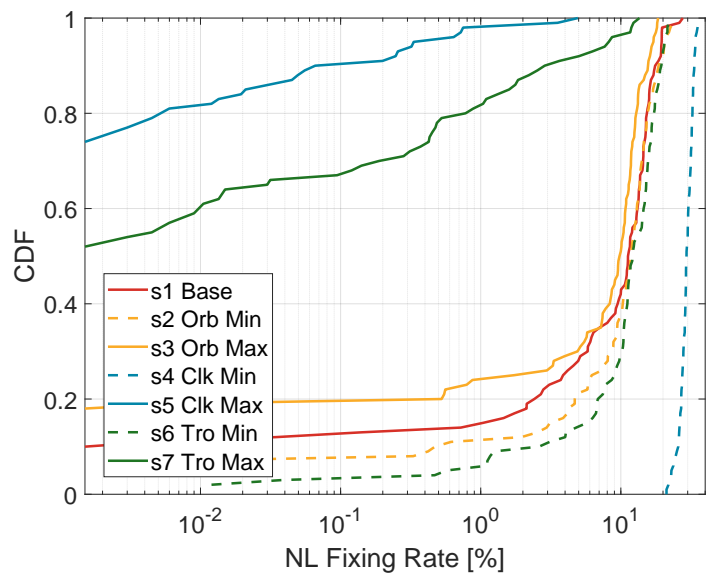(b) AR Model (Low Autocorrelation)

(c) AR Model (High Autocorrelation)

Figure 5.5: *Cumulative Distribution of Wide Lane Fixing Rate Across Varying Residual Simulation Models*
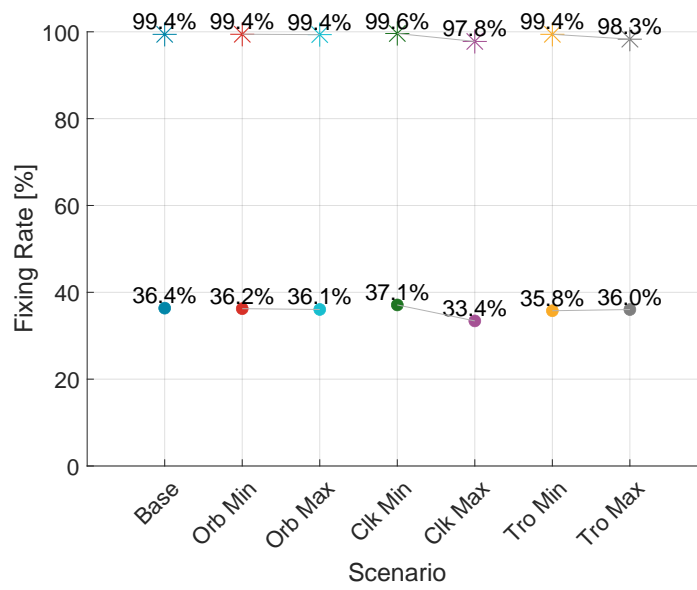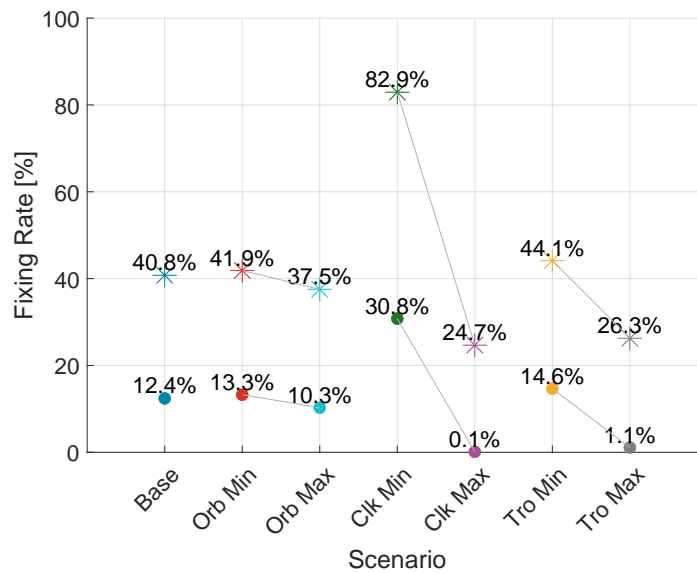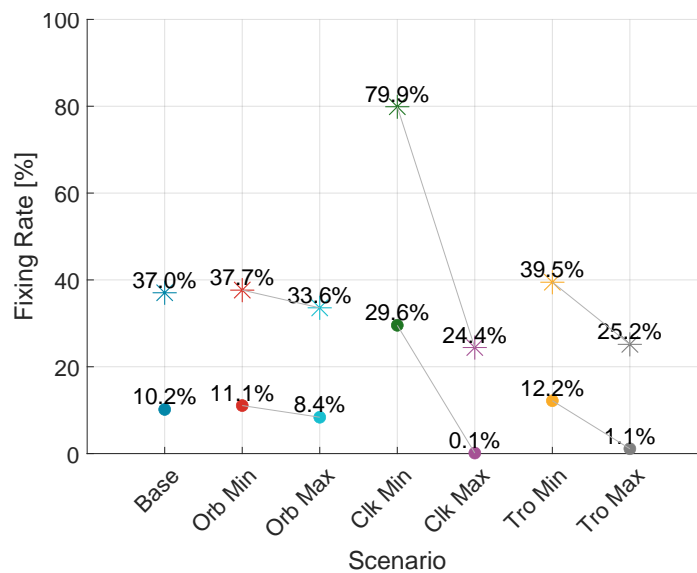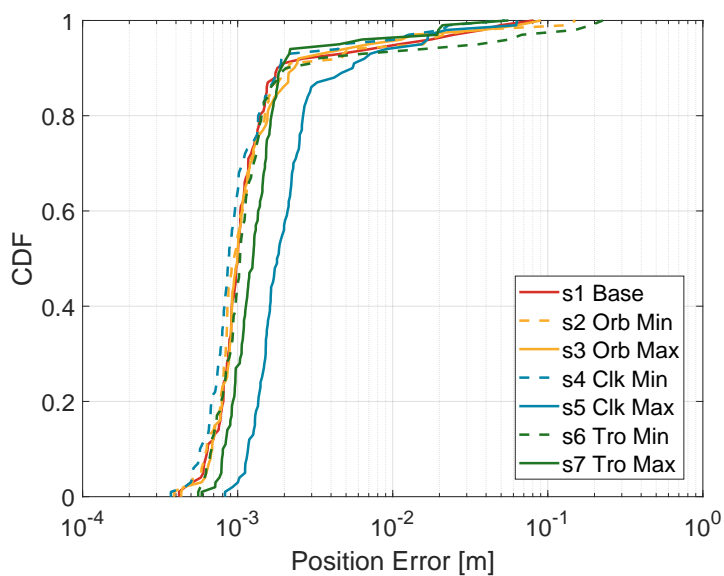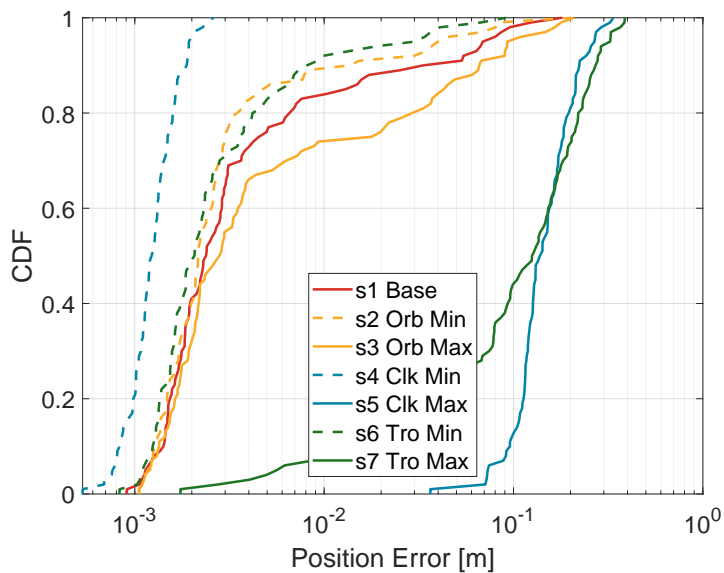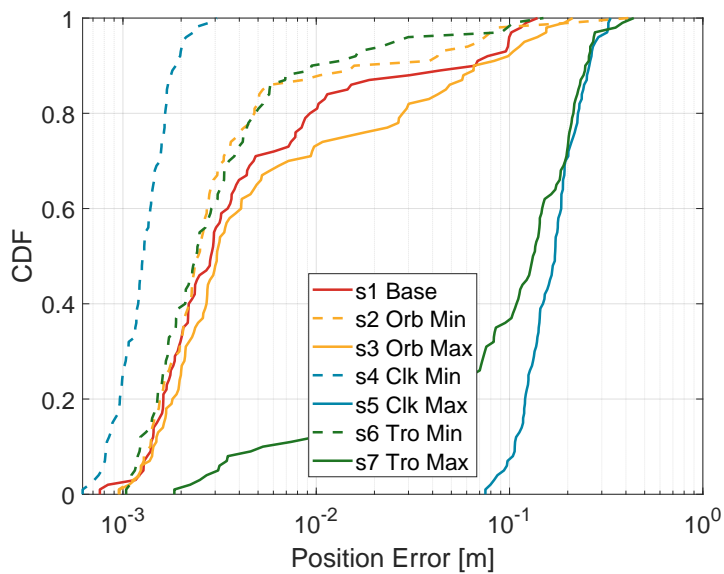
(a) Gaussian Model

(b) AR Model (Low Autocorrelation)

(c) AR Model (High Autocorrelation)

Figure 5.6: *Cumulative Distribution of Narrow Lane Fixing Rate Across Varying Residual Simulation Models*

(a) Gaussian Model

(b) AR Model (Low Autocorrelation)

(c) AR Model (High Autocorrelation)

Figure 5.7: *Cumulative Distribution of Averaged Fixing Rate Across Varying Residual Simulation Models:* ⋆
denotes WL, and · refers to NL

(a) Gaussian Model

(b) AR Model (Low Autocorrelation)

(c) AR Model (High Autocorrelation)

Figure 5.8: *Cumulative Distribution of 2D Position Error Across Varying Residual Simulation Models*

While the above KPIs support the similarity in the findings, there are also inconsistencies. As mentioned earlier, the anomaly in scenario 4 also becomes apparent in both Wide lane and narrow lane fixing rate area. Probably, the base setting for the clock standard is too high, making it the dominant factor. This leads to the situation where even other error standards may change, but their impact is not as significant compared to the dominant effect. Furthermore, there is a sudden drop in the wide-lane fixing rate for all scenarios except Scenario 4 (s4). The reason behind this is a strict threshold of 0.12. If the difference is too significant before rounding, the wide-lane will not exceed the threshold. Unfortunately, the new model AR tends to remain in these awkward situations.

Concerning the position error illustrated in Figure 5.8, it is clear that the Gaussian model offers a notably more accurate 2D position compared to the AR model, which displays lower precision. In reality, the residuals are more intricate, and the Gaussian model alone may not suffice. The behavior of the AR model seems to align more closely with reality. Specifically within the AR model, the position error appears to be particularly influenced by tropospheric error groups. Additionally, an increase in autocorrelation is associated with a decrease in positional precision.

In brief, the AR model exhibits potential for representing future trends by capturing the behavior of residuals.

5.3 Exploring the Influence of Phase Noise Levels in AR Model

To delve into a more profound comprehension of the influence of phase noise on the performance metrics of Convergence Time, Fixing Rate, and Position Errors, we meticulously maintain the consistency of the methodology. This is achieved by keeping the residuals and noise on code measurement constant. Following this, we introduce varying levels of noise specifically for the phase measurement component. Subsequent analyses explore the impact of phase noise on key performance indicators, as depicted in Figures 5.9, 5.10, 5.11, 5.12, and 5.13.

Figures 5.9 illustrate the effects of variations in phase noise on the cumulative distribution function of convergence time. The three overall plots do not distinctly showcase the impact, as they demonstrate a similar trend.

These figures warrant closer examination to elucidate the impact of phase noise on fixation rates. Unfortunately, Figure 5.10 reveals only minimal significant differences, suggesting that the noise level has a marginal influence on the wide lane fixing rate. However, a notably more pronounced change is observed in Figure 5.11. Here, the narrow lane fixing rate demonstrates a significant decrease, corresponding with an increase in phase noise.

To offer a more comprehensive understanding, Figure 5.12 presents both wide lane and narrow lane mean mean fixing rate values. Further reference to this figure is recommended for the reader. These mean values provide a comprehensive narrative that aligns with previous observations. The observed decrease in the narrow lane fixing rate, occurring alongside increased phase noise, is thus corroborated and reflected in these mean values.
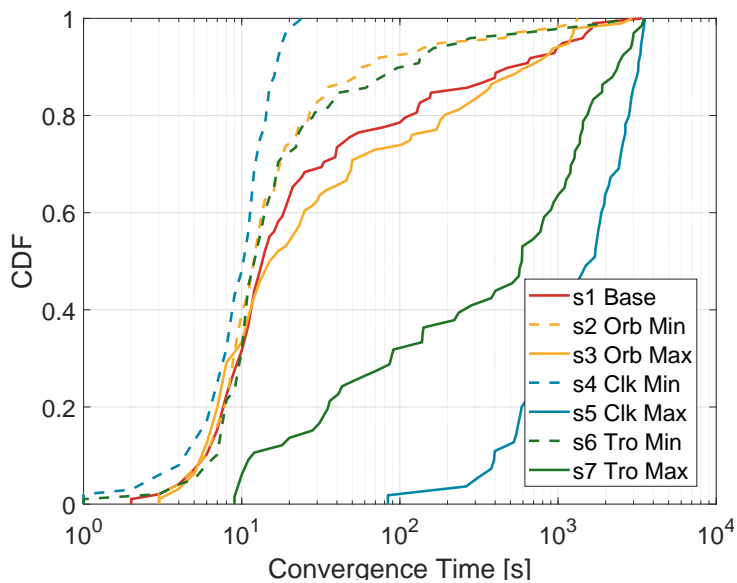
Concerning the CDFs of the positional errors, as illustrated in Figure 5.13, the discerned impact continues to exhibit a somewhat subdued manifestation. Despite the perturbations introduced
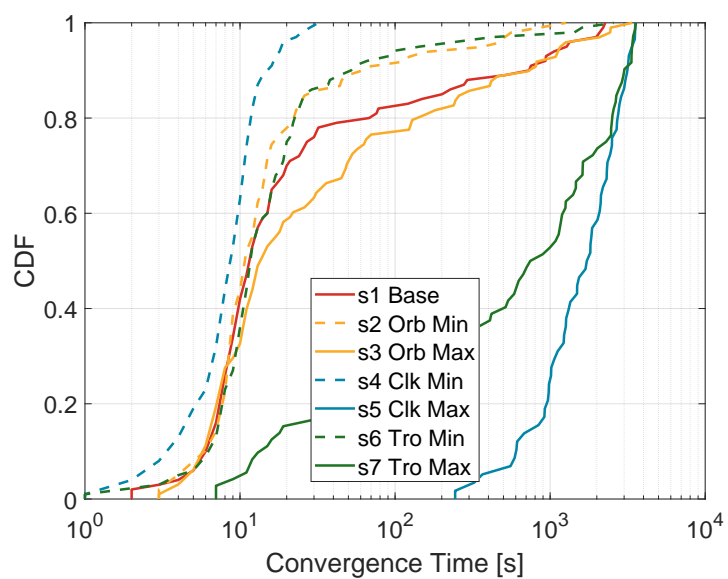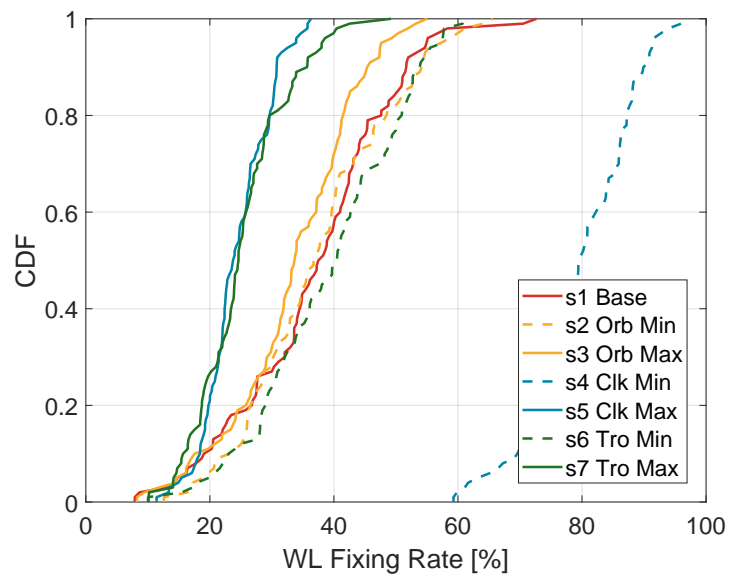
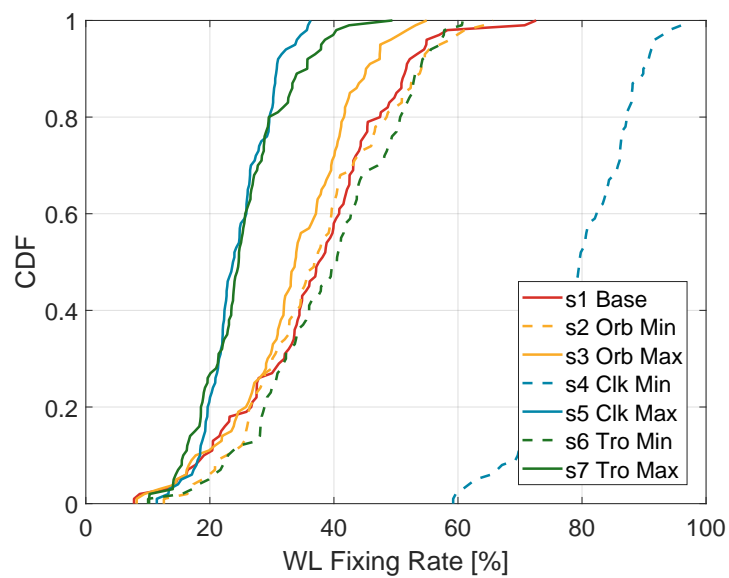(a) AR Model of 4 mm Phase Noise
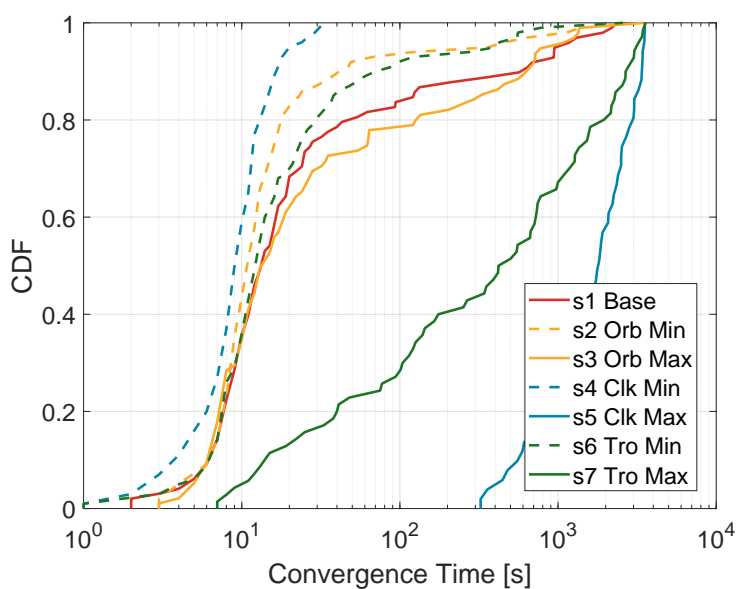
(b) AR Model of 8 mm Phase Noise

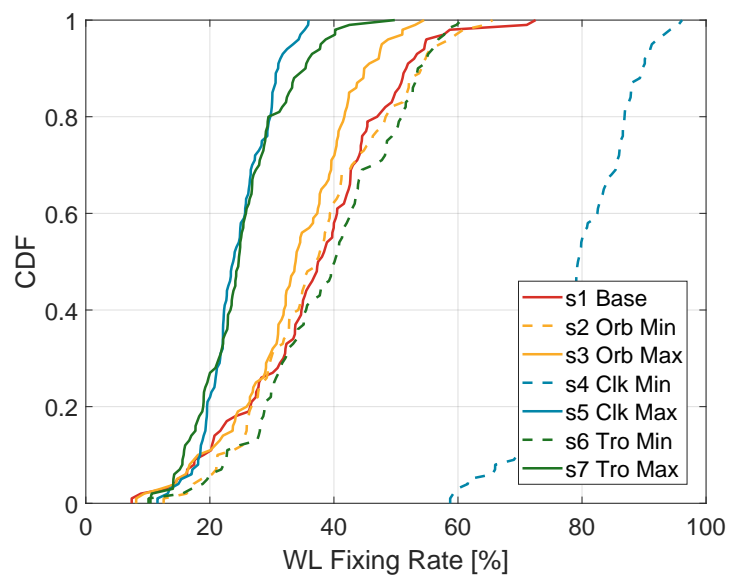

(c) AR Model of 20 mm Phase Noise

Figure 5.9: *Cumulative Distribution of Convergence Time Across Varying Phase Noise*

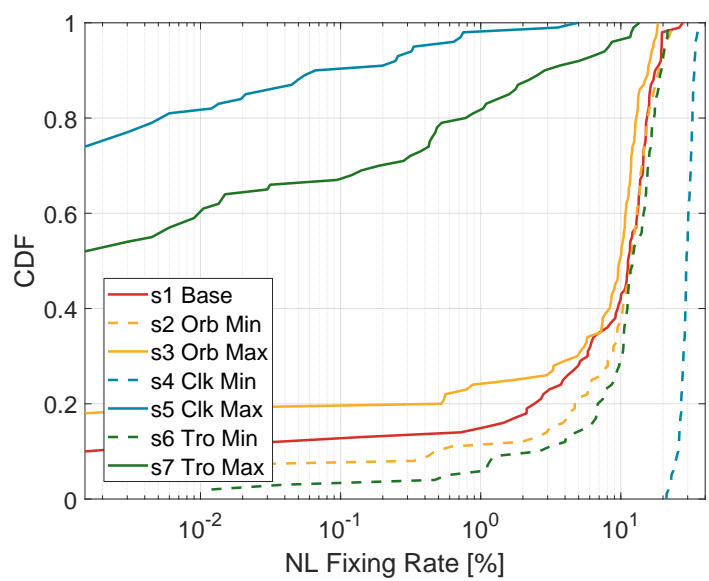(a) AR Model of 4 mm Phase Noise
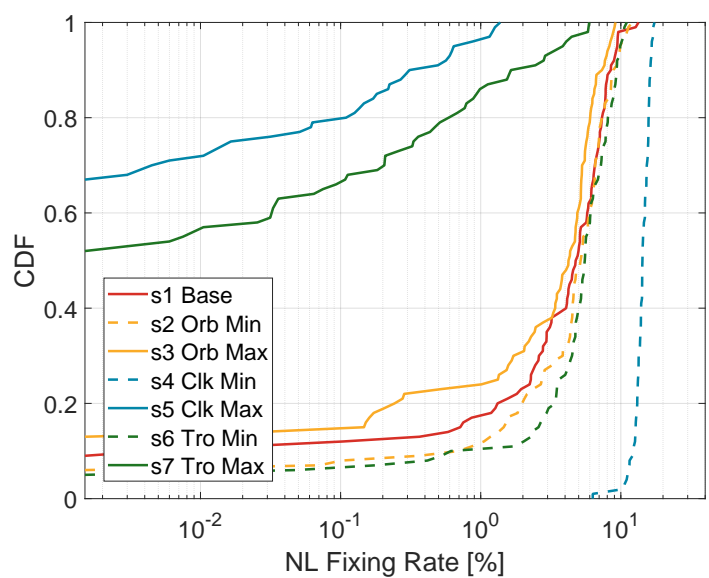

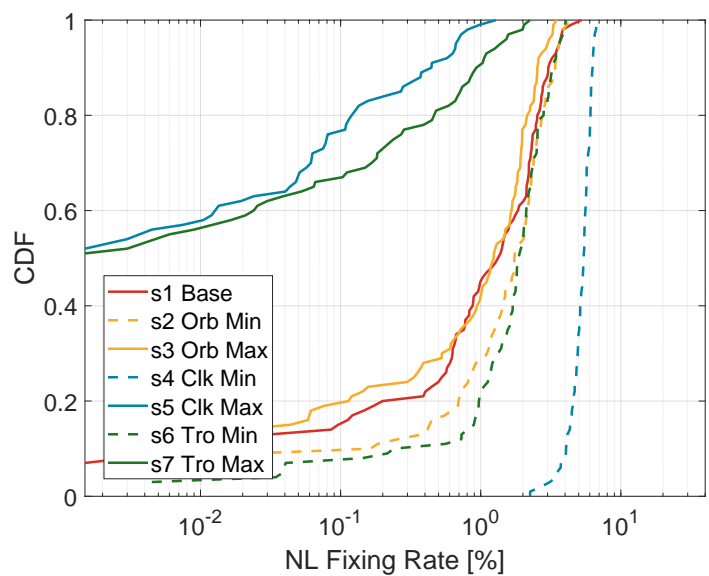(b) AR Model of 8 mm Phase Noise

(c) AR Model of 20 mm Phase Noise

Figure 5.10: *Cumulative Distribution of Wide Lane Fixing Rate Across Varying Phase Noise*

(a) AR Model of 4 mm Phase Noise

(b) AR Model of 8 mm Phase Noise

(c) AR Model of 20 mm Phase Noise

Figure 5.11: *Cumulative Distribution of Narrow Lane Fixing Rate Across Varying Phase Noise*
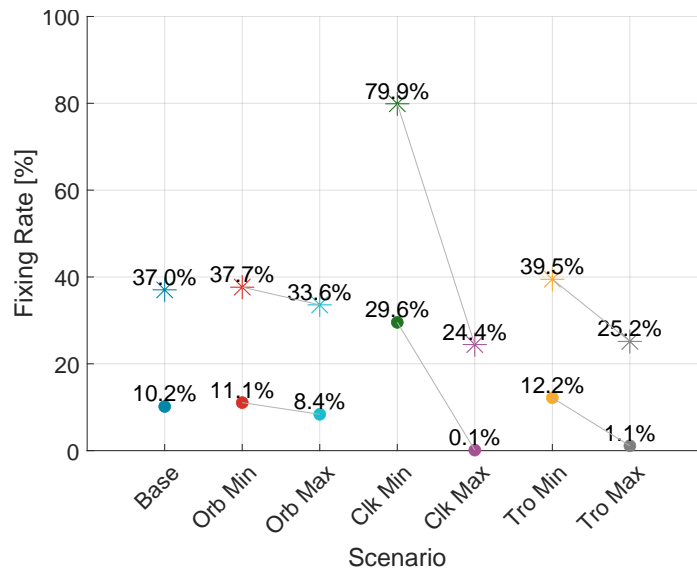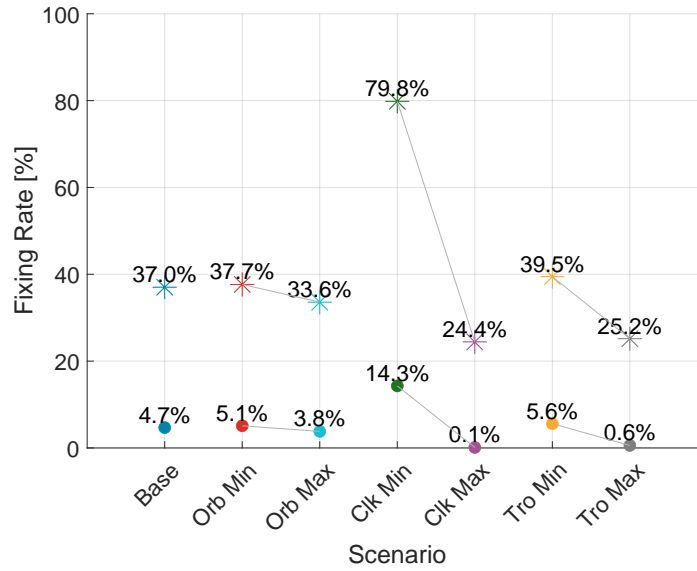
(a) AR Model of 4 mm Phase Noise

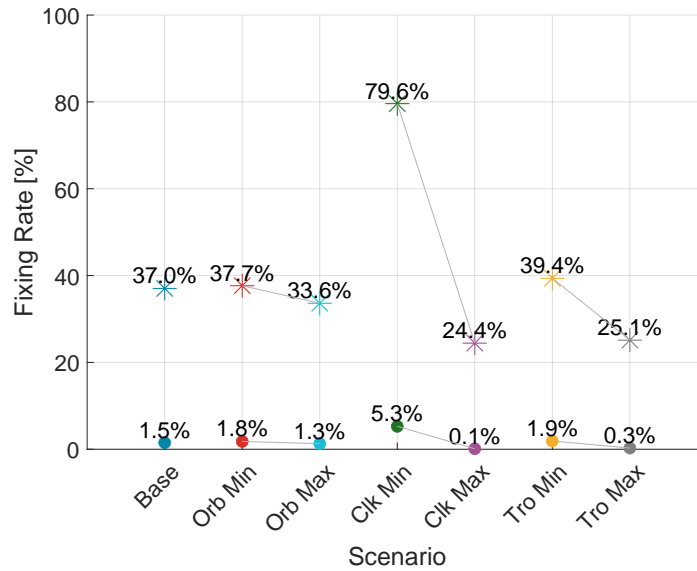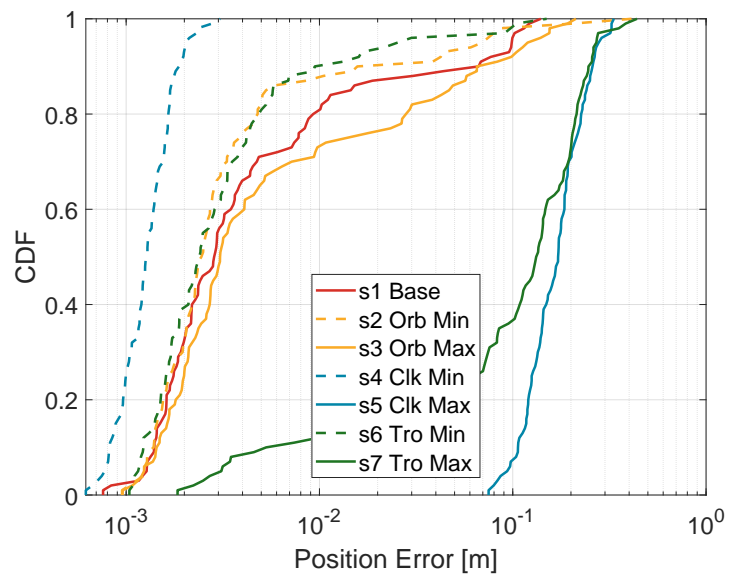(b) AR Model of 8 mm Phase Noise

(c) AR Model of 20 mm Phase Noise

Figure 5.12: *Cumulative Distribution of Narrow Lane Fixing Rate Across Varying Phase Noise: ⋆ denotes WL, and · refers to NL*

by varying levels of phase noise, the overarching influence on the distribution of positional errors appears to remain relatively restrained. The variations depicted in the CDFs intimate a not pronounced shift in the distribution characteristics, thereby seeming to reinforce the assumption that the impact of phase noise on positional errors is not overtly significant. Additionally, the observed trend suggests that the inherent resilience of positioning accuracy, as depicted by the CDFs, attests to the robustness of the underlying correction mechanisms against the introduced perturbations in the form of phase noise.

Conversely, it is imperative to note that in reality, this observation may not hold true. It is a commonly known fact that, generally, less noise leads to higher position error. Further discussions are needed to delve into this apparent contradiction and reconcile it with established knowledge in the field.

The observed phenomenon may be attributed to the convergence condition. To validate this assumption, we also present the position error, as shown in Figure 5.14, relative to the epochs. The greater the phase noise, the higher the tendency for position error. The selected range for phase noise is from 4 mm to 20 mm, impacting the results but failing to make it distinct. For instance, regarding the convergence time, we set it at 10 cm. This means that only position errors below 10 cm for 10 min are considered as converged. It is evident that the magnitude of the phase noise's impact on position error is significantly less compared to 10 cm.

Upon comparing these conditions, it becomes clear that the impact introduced by the phase noise change is minimal. We can only observe a small change because our threshold is larger. This discrepancy could provide a plausible explanation for the limited impact of phase noise variations on the cumulative distribution function of convergence time and position error.

(a) AR Model of 4 mm Phase Noise
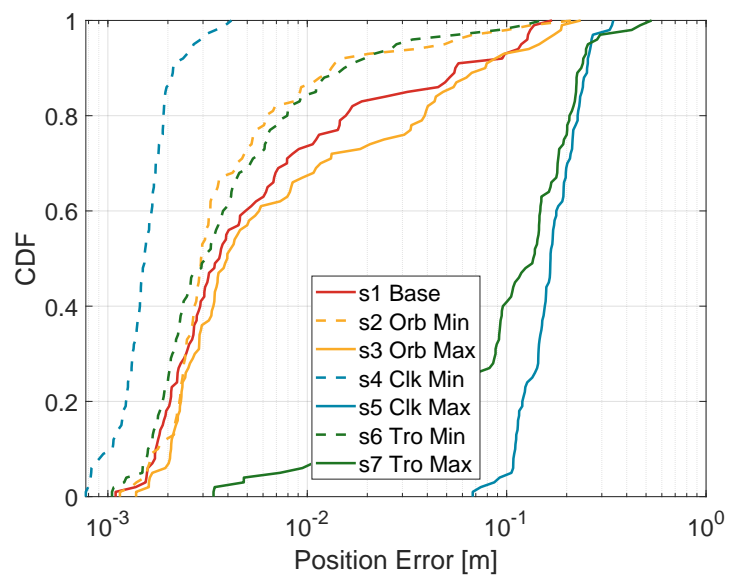
(b) AR Model of 8 mm Phase Noise
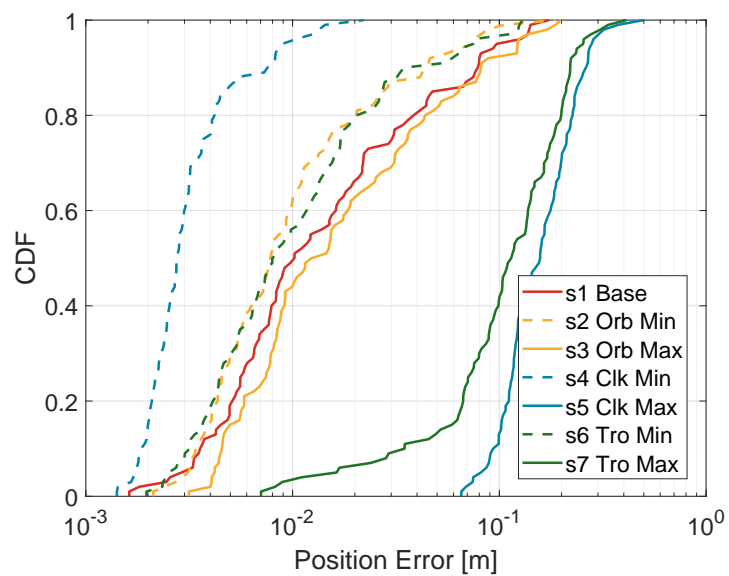
(c) AR Model of 20 mm Phase Noise

Figure 5.13: *Cumulative Distribution of 2D Position Error Across Varying Phase Noise*

(a) AR Model of 4 mm Phase Noise

(b) AR Model of 8 mm Phase Noise

(c) AR Model of 20 mm Phase Noise

Figure 5.14: *Dynamic Trend of 2D Position Error Across Varying Phase Noise*

Chapter 6

Conclusions and Outlook

6.1 Summary and Conclusion

The ascent of PPP as a prominent method in the GNSS field has garnered significant attention. PPP, a technique for determining positions without nearby reference statio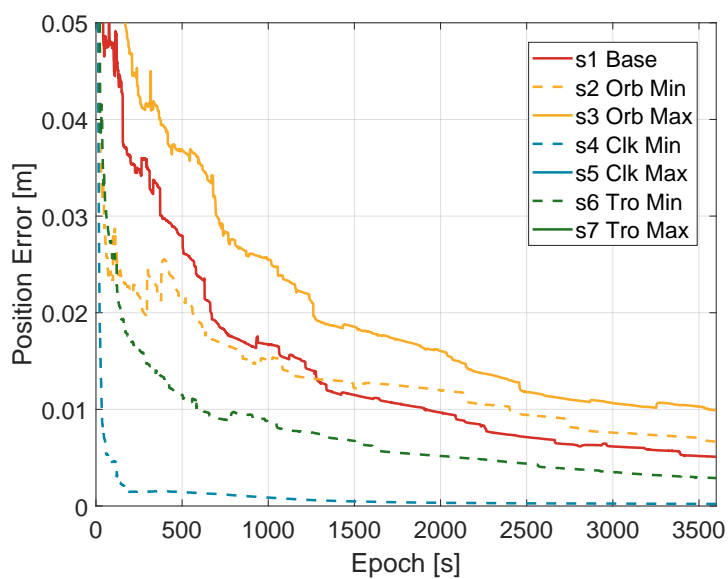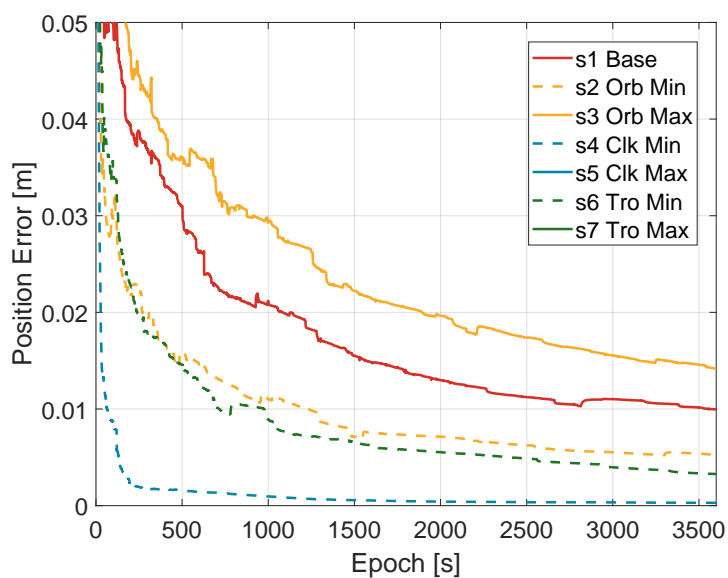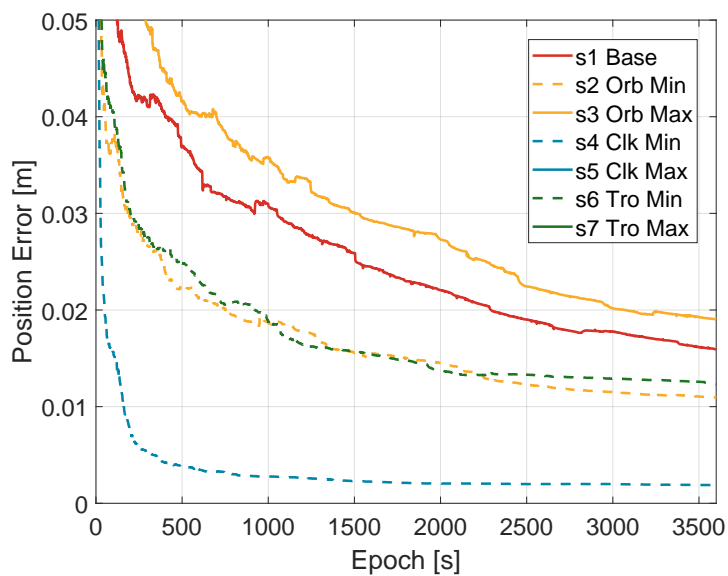ns, exhibits high precision, reaching centimeter-level accuracy in kinematic mode and millimeter-level accuracy in static mode after convergence. This precision is achieved with the aid of high-precision satellite orbit, clock products, and atmospheric products. Despite its convenience and accuracy, the lingering issue of convergence time persists, often extending to minutes or even tens of minutes in practical scenarios. Additionally, correction products, typically considered deterministic. Nevertheless, in practice, these factors introduce uncertainties that can impact their reliability, potentially leading to suboptimal KPIs.

The primary objective of this research is to assess the sensitivity of convergence time, fixing rate, and position error to the changes in the accuracy of correction products for various error sources, including satellite orbit errors, satellite clock errors, and tropospheric errors. By discerning this information, we can identify specific products that require greater precision, thereby significantly enhancing convergence time or other KPIs in future endeavors.

To achieve this goal, we utilize the PPP AR Engine. This engine employs a combination of Wide Lane and Narrow Lane observations in its algorithm. Additionally, it uses the least squares method to furnish the initial values for the Kalman filter state vector in subsequent steps. It is crucial to observe that the Wide Lane ambiguity fixing condition serves as an indicator for determining whether to subsequently employ the conventional IF combination or the NL combination. Empirical tests, such as the residual test, introduce stringent conditions that may result in a lower fixing rate compared to other research methodologies. In practical scenarios, isolating the error source of interest poses a challenge due to inherent correlations among different sources.

To effectively manage and control errors, such as the error sources and their magnitude, simulated data is employed in this context. The simulated data incorporates various error components, including satellite orbit errors, satellite clock errors, and tropospheric errors derived from correction products. Additionally, simulations are conducted under open-sky conditions' multipath and tracking noises to assess the impact of different correction products. In other words, the code measurement considers factors such as multipath and specific noises. For phase measurements, the focus is only on incorporating specific noises within the certain range. Except for the error sources mentioned earlier, such as multipath and noises, no additional error sources, e.g, antenna phase-related errors or biases, are introduced into the experiment.

To this end, two correction residuals models have been introduced to emulate the behavior of persistent errors or uncertainties within correction products: the White Gaussian model and the AR model. It is important to note that the AR model employed is a simplified 1st-order model, and the selection of parameters is based on our empirical experience.

The study undertakes comparisons among uncertainties change in the correction product for diverse error sources. The "Base" scenario represents error magnitudes at an intermediate level, while "Min" and "Max" values signify the corresponding correction product uncertainties as either small or large. Furthermore, the thesis presents a comparative analysis of various error uncertainty simulation models, specifically the Gaussian model and AR model. Their performance is evaluated in terms of convergence time, Wide Lane fixing rate, Narrow Lane fixing rate, and position error. Subsequently, the thesis delves into a contrast of AR model parameter choices, with a primary focus on the autocorrelation of the data and its impact on the KPIs. Finally, the paper explores the influence of phase noise ranging from 4 mm to 20 mm, while maintaining consistent magnitudes of errors in code measurements.

In conclusion, our research has revealed several key insights:

- In the absence of biases and when employing correction products from other error sources, the convergence time can be remarkably short, often taking about 10 s.

- Sensitivity analysis indicated that the convergence time, fixing rate, and position error are most affected by satellite clock standard deviation variations, followed by the troposphere and orbit errors under consistent experimental conditions. For instance, in the Gaussian model with 1000 runs at the 68th percentile, the difference between the minimum and maximum standard deviations scenarios for the satellite clock error group, troposphere group, and orbital error group is observed as 21 s, 5 s, and 1 s, respectively, in terms of convergence time.

- White Gaussian and AR models partially capture the residual behavior of enhanced products, with a greater emphasis on AR models.

- In the AR model, an increase in the autocorrelation of errors is associated with a decline in KPIs performance. Specifically, when the autocorrelation ranges from non-autocorrelated to highly autocorrelated, the convergence times at the 68th percentile in the "Base" scenario exhibit values of approximately 13 s, 18 s, and 20 s for the three different conditions. The WL fixing rates for these conditions are 99%, 46%, and 43%, while the NL fixing rates are 38%, 15%, and 14%, respectively. Additionally, the average 2D position errors for the "Base" scenario are measured at 0.003 m, 0.012 m, and 0.015 m.

- While variations in phase noise typically lead to performance degradation, considering the looser KPI conditions, this effect may be obscured, potentially leading to a false assumption that it is trivial to the performance. For the "Base" scenario, when phase noises are 4 mm, 8 mm, and 20 mm, the convergence times at the 68th percentile for these three conditions are 20 s, 20 s, and 26 s, respectively. The WL fixing rates for all three conditions are approximately 42%, while the NL fixing rates are 14%, 6%, and 2%. Notably, accuracy decrease in 2D mean position error is observed, measuring 0.015 m, 0.019 m, and 0.027 m for the respective noise levels.

However, the study has certain limitations. The investigations often neglect the propagation of residuals or uncertainties through the model onto phase measurements. Additionally, due to

time and data constraints, factors such as phase and code biases, antenna Phase Center Offset and Phase Center Variations, have not been thoroughly discussed. The focus on correction products in the line of sight may be overly simplistic, considering challenges in translating orbit products from ECEF to line of sight.

The reference values used in the experiment primarily pertain to GPS and GLONASS. Nevertheless, it is crucial to note that other constellations, such as Galileo and Beidou navigation systems, may exhibit varying correction product accuracies. Therefore, consideration of different constellations becomes imperative. In addition, AR model parameters, such as constant time and the order of AR, based on empirical experience, might not be sufficient to reflect the actual behavior of the residuals and noise.

Overall, this thesis presents a fresh perspective on PPP analysis, highlighting the significance of correction product behavior and the potential advantages of utilizing high-precision products to improve PPP AR performance. While recognizing certain limitations, it also suggests directions for future research, thereby offering valuable insights to the broader field of PPP.

6.2 Future Work: Enhancing the Prospects of the Thesis

To enhance the model's ability to express the residual behavior of correction products, several considerations can be explored in future research:

- The residual test serves well in ensuring a stable fixed ambiguity, yet its strictness might result in the rejection of potentially accurate values, leading to a lower fixing rate without contributing to enhanced system performance. Moreover, the chosen values are primarily based on empirical experience. To address this, conduct experiments with the aim of fine-tuning residual test conditions to achieve higher precision.

- Utilize authentic correction datasets, such as those from IGS or SwiftNav, to infer optimal AR model parameters. Consider integrating Artificial Intelligence for this aspect.

- Due to constraints in time and resources, the majority of the work was limited to 100 runs. However, for more robust and stable results, it is recommended to broaden the scope of experimental simulations.

- Explore potential research avenues, including the uncertainty of correction products or the analysis of error behavior in phase and code measurements.

- While the current findings are grounded in static mode, delve into discussions regarding the dynamic model as well.

- Deduce the real values of standards of products in the line of sight through correction products to provide a more accurate representation.

- As mentioned earlier, the study has primarily focused on orbital errors, satellite clock errors, troposphere errors, multipath, and noise. However, real-world situations are more intricate. To enhance the study's comprehensiveness, delve into additional error sources, including the examination of biases and the impact of ionosphere delay.

Bibliography

A. Becker. Kalman filter. *Dipetik Juli*, 1:2020, 2018.

H. Berg. Allgemeine meteorologie: Einführung in die physik der atmosphäre. *(No Title)*, 1948.

S. Bisnath and Y. Gao. Current state of precise point positioning and future prospects and limitations. In *Observing our changing earth*, pages 615–623. Springer, 2009.

G. Blewitt. An automatic editing algorithm for gps data. *Geophysical research letters*, 17(3):199–202, 1990.

P. Bona. Precision, cross correlation, and time correlation of gps phase and code observations. *GPS solutions*, 4:3–13, 2000.

X. W. Chang, X. Yang, and T. Zhou. Mlambda: A modified lambda method for integer least-squares estimation. *Journal of Geodesy*, 79:552–565, 2005.

J. Chen, H. Li, B. Wu, Y. Zhang, J. Wang, and C. Hu. Performance of real-time precise point positioning. *Marine Geodesy*, 36(1):98–108, 2013.

S. Choy, S. Bisnath, and C. Rizos. Uncovering common misconceptions in gnss precise point positioning and its future prospect. *GPS solutions*, 21:13–22, 2017.

J. Cisak and Y. M. Zanimonskiy. Results of the investigations of the gnss antennae in the framework of scar giant project ‚Äúin situ gnss antenna tests and validation of phase centre calibration data‚Äù. In *Geodetic and Geophysical Observations in Antarctica: An Overview in the IPY Perspective*, pages 179–190. Springer, 2008.

B. Cui, J. Wang, P. Li, M. Ge, and H. Schuh. Modeling wide-area tropospheric delay corrections for fast ppp ambiguity resolution. *GPS Solutions*, 26(2):56, 2022.

J. Davis, T. Herring, I. Shapiro, A. Rogers, and G. Elgered. Geodesy by radio interferometry: Effects of atmospheric modeling errors on estimates of baseline length. *Radio science*, 20(6):1593–1607, 1985.

A. I. EL-Hattab. Influence of gps antenna phase center variation on precise positioning. *NRIAG Journal of Astronomy and Geophysics*, 2(2):272–277, 2013.

A. El-Mowafy. Precise real-time positioning using network rtk. *Global navigation satellite systems: signal, theory and applications*, 7:161–88, 2012.

A. El-Rabbany. *Global Positioning System*. Artech House Publishers, 2002.

M. Elsheikh, W. Abdelfatah, A. Noureldin, U. Iqbal, and M. Korenberg. Low-cost real-time ppp/ins integration for automated land vehicles. *Sensors*, 19(22):4896, 2019.

M. Elsheikh, U. Iqbal, A. Noureldin, and M. Korenberg. The implementation of precise point positioning (ppp): A comprehensive review. *Sensors*, 23(21):8874, 2023.

M. Elsobeiey and S. Al-Harbi. Performance of real-time precise point positioning using igs real-time service. *GPS solutions*, 20:565–571, 2016.

European Union Agency for the Space Programme. What is GNSS?, 2023. URL `https://www.euspa.europa.eu/european-space/eu-space-programme/what-gnss`. Accessed: November 17, 2023.

Y. Gao and K. Chen. Performance analysis of precise point positioning using real-time orbit and clock products. *Journal of Global Positioning Systems*, 3(1-2):95–100, 2004.

Z. Gao, H. Zhang, M. Ge, X. Niu, W. Shen, J. Wickert, and H. Schuh. Tightly coupled integration of multi-gnss ppp and mems inertial measurement unit data. *GPS solutions*, 21:377–391, 2017.

M. Ge, G. Gendt, M. a. Rothacher, C. Shi, and J. Liu. Resolution of gps carrier-phase ambiguities in precise point positioning (ppp) with daily observations. *Journal of geodesy*, 82:389–399, 2008.

J. Geng and C. Shi. Rapid initialization of real-time ppp by resolving undifferenced gps and glonass ambiguities simultaneously. *Journal of Geodesy*, 91:361–374, 2017.

A. Hauschild. Basic observation equations. *Springer handbook of global navigation satellite systems*, pages 561–582, 2017.

A. Hauschild and O. Montenbruck. Kalman-filter-based gps clock estimation for near real-time positioning. *GPS solutions*, 13:173–182, 2009.

J. M. Hebert. Velocity determination for an inverted pseudolite navigation reference system. Master's thesis, Air Force Institute of Technology, 1995.

Ž. Hećimović. Relativistic effects on satellite navigation. *Technical Gazette*, 20(1):195–203, 2013.

H. Hopfield. The effect of tropospheric refraction on the doppler shift of a satellite signal. *Journal of Geophysical Research*, 68(18):5157–5168, 1963.

IGS. Igs products, 2022. URL `https://igs.org/products/#orbits_clocks`.

J. Kouba. A guide to using international gnss service (igs) products, 2009.

K. Lagler, M. Schindelegger, J. Böhm, H. Krásná, and T. Nilsson. Gpt2: Empirical slant delay model for radio space geodetic techniques. *Geophysical research letters*, 40(6):1069–1073, 2013.

L. Li, J. Zhong, and M. Zhao. Doppler-aided gnss position estimation with weighted least squares. *IEEE transactions on vehicular technology*, 60(8):3615–3624, 2011.

T. Li, J. Wang, and D. Laurichesse. Modeling and quality control for reliable precise point positioning integer ambiguity resolution with gnss modernization. *GPS solutions*, 18:429–442, 2014a.

X. Li, M. Ge, J. Douša, and J. Wickert. Real-time precise point positioning regional augmentation for large gps reference networks. *GPS solutions*, 18:61–71, 2014b.

X. Li, X. Li, G. Liu, G. Feng, Y. Yuan, K. Zhang, and X. Ren. Triple-frequency ppp ambiguity resolution with multi-constellation gnss: Bds and galileo. *Journal of Geodesy*, 93:1105–1122, 2019.

X. Li, G. Liu, X. Li, F. Zhou, G. Feng, Y. Yuan, and K. Zhang. Galileo ppp rapid ambiguity resolution with five-frequency observations. *GPS Solutions*, 24:1–13, 2020.

S. Liu, F. Sun, L. Zhang, W. Li, and X. Zhu. Tight integration of ambiguity-fixed ppp and ins: model description and initial results. *GPS solutions*, 20(1):39–49, 2016.

Y. Liu, U. Hugentobler, B. Duan, N. Mikhaylov, and J. Simon. Receiver bias estimation strategy in the uncombined triple-frequency ppp-ar model. pages 2570–2580, 10 2023a. doi:10.33012/2023.19220.

Y. Liu, N. Mikhaylov, U. Hugentober, and B. Duan. Triple-frequency ppp-ar model comparison from the user perspective: combined and uncombined models. In *2023 IEEE/ION Position, Location and Navigation Symposium (PLANS)*, pages 867–874, 2023b. doi:10.1109/PLANS53410.2023.10139924.

K. M. A. Mageed. Accuracy evaluation between gps virtual reference station (vrs) and gps real time kinamatic (rtk) techniques. *World Appl. Sci. J*, 24:1154–1162, 2013.

J. W. Marini. Correction of satellite tracking data for an arbitrary tropospheric profile. *Radio Science*, 7(2):223–231, 1972.

O. Montenbruck and A. Hauschild. Code biases in multi-gnss point positioning. In *Proceedings of the 2013 International Technical Meeting of The Institute of Navigation*, pages 616–628, 2013.

O. Montenbruck, P. Steigenberger, R. Khachikyan, G. Weber, R. Langley, L. Mervart, and U. Hugentobler. Igs-mgex: preparing the ground for multi-constellation gnss science. *Inside Gnss*, 9(1):42–49, 2014.

E. Necôulescu. Performance analysis of the low-cost gnss receivers based on the ppp techniques. 2022.

D. Odijk, P. J. Teunissen, and A. Khodabandeh. Single-frequency ppp-rtk: theory and experimental results. In *Earth on the Edge: Science for a Sustainable Planet: Proceedings of the IAG General Assembly, Melbourne, Australia, June 28-July 2, 2011*, pages 571–578. Springer, 2014.

C. A. Ogaja. Introduction to gnss geodesy.

L. Pan, B. Xiong, X. Li, W. Yu, and W. Dai. High-rate gnss multi-frequency uncombined ppp-ar for dynamic deformation monitoring. *Advances in Space Research*, 72(10):4350–4363, 2023.

J. Rankin. Gps and differential gps: An error model for sensor simulation. In *Position Location and Navigation Symposium*, pages 260–260. INSTITUTE OF ELECTRICAL & ELECTRONICS ENGINEERS INC, 1994.

C. Rizos and S. Han. Reference station network based rtk systems-concepts and progress. *Wuhan University Journal of Natural Sciences*, 8:566–574, 2003.

J. Saastamoinen. Atmospheric correction for the troposphere and stratosphere in radio ranging satellites. *The use of artificial satellites for geodesy*, 15:247–251, 1972.

R. F. SC-159. *Minimum operational performance standards for global positioning system/wide area augmentation system airborne equipment*. RTCA, 2006.

T. Takasu and A. Yasuda. Development of the low-cost rtk-gps receiver with an open source program package rtklib. In *International symposium on GPS/GNSS*, volume 1, pages 1–6. International Convention Center Jeju Korea Seogwipo-si, Republic of Korea, 2009.

P. J. Teunissen. Least-squares estimation of the integer gps ambiguities. In *Invited lecture, section IV theory and methodology, IAG general meeting, Beijing, China*, pages 1–16, 1993.

P. J. Teunissen and O. Montenbruck. *Springer handbook of global navigation satellite systems*, volume 10. Springer, 2017.

P. Teunnissen. The least-square ambiguity decorrelation adjustment: a method for fast gps integer ambiguity estimation. *J. Geodesy*, 70(1):65–82, 1995.

A. Verhagen. The gnss integer ambiguities: Estimation and validation. 2004.

S. Verhagen, B. Li, and M. Geodesy. Lambda software package: Matlab implementation, version 3.0. *Delft University of Technology and Curtin University, Perth, Australia*, 2012.

G. Wabbena, M. Schmitz, and A. Bagge. Ppp-rtk: precise point positioning using state-space representation in rtk networks. In *Proceedings of the 18th international technical meeting of the satellite division of the Institute of navigation (ION GNSS 2005)*, pages 2584–2594, 2005.

Wikipedia contributors. Autoregressive model, 2023. URL `https://en.wikipedia.org/wiki/Autoregressive_model`. Accessed: [Insert Date].

J. Xiong and F. Han. Positioning performance analysis on combined gps/bds precise point positioning. *Geodesy and Geodynamics*, 11(1):78–83, 2020.

K. Yedukondalu, A. D. Sarma, and S. S. Vemuri. Estimation and mitigation of gps multipath interference using adaptive filtering. *Progress in electromagnetics research m*, 21:133–148, 2011.

B. Zhang, P. J. Teunissen, and D. Odijk. A novel un-differenced ppp-rtk concept. *The Journal of Navigation*, 64(S1):S180–S191, 2011.

B. Zhang, J. Ou, Y. Yuan, and Z. Li. Extraction of line-of-sight ionospheric observables from gps data using precise point positioning. *Science China Earth Sciences*, 55:1919–1928, 2012.

C. Zhang. Accuracy assessment of kinematic precise point positioning with triple gnss constellation. Master's thesis, University of Stuttgart, 2020.

J. Zhang, M. Wu, T. Li, and K. Zhang. Integer aperture ambiguity resolution based on difference test. *Journal of geodesy*, 89:667–683, 2015.

X. Zhang, F. Guo, and P. Zhou. Improved precise point positioning in the presence of ionospheric scintillation. *GPS solutions*, 18:51–60, 2014.

X. Zhang, X. Li, and P. Li. Review of gnss ppp and its application. *Acta Geodaetica et Cartographica Sinica*, 46(10):1399–1407, 2017. doi:10.11947/j.AGCS.2017.20170327.

X. Zhang, X. Ren, J. Chen, X. Zuo, D. Mei, and W. Liu. Investigating gnss ppp–rtk with external ionospheric constraints. *Satellite navigation*, 3(1):1–13, 2022.

J. Zumberge, M. Heflin, D. Jefferson, M. Watkins, and F. Webb. Precise point positioning for the efficient and robust analysis of gps data from large networks. *Journal of geophysical research: solid earth*, 102(B3):5005–5017, 1997.